IRAQI JOURNAL OF APPLIED PHYSICS

The *Iraqi Journal of Applied Physics (IJAP)* is a peer reviewed journal of high quality devoted to the publication of original research papers from applied physics and their broad range of applications. IJAP publishes quality original research papers, comprehensive review articles, survey articles, book reviews, dissertation abstracts in physics and its applications in the broadest sense. It is intended that the journal may act as an interdisciplinary forum for Physics and its applications. Innovative applications and material that brings together diverse areas of Physics are particularly welcome. Review articles in selected areas are published from time to time. It aims to disseminate knowledge; provide a learned reference in the field; and establish channels of communication between academic and research experts, policy makers and executives in industry, commerce and investment institutions. IJAP is a quarterly specialized periodical dedicated to publishing original papers, letters and reviews in: Applied & Nonlinear Optics, Applied Mechanics & Thermodynamics, Digital & Optical Communications, Electronic Materials & Devices, Laser Physics & Applications, Plasma Physics & Applications, Quantum Physics & Spectroscopy, Semiconductors & Optoelectronics, Solid State Physics & Applications, Alternative and Renewable Energy, and Computers and Networks.

ISSN (Print): 1813-2065, ISSN (Online): 2309-1673, ISSN (Letters): 1999-656X

EDITORIAL BOARD

Editorial Office:
P. O. Box 55259, Baghdad 12001, IRAQ
Website: www.iraqiphysicsjournal.com
Emails: info@iraqiphysicsjournal.com, editor_ijap@yahoo.co.uk, editor@ijaponline.com

ADVISORY BOARD

SPONSORED AND PUBLISHED BY
THE IRAQI SOCIETY FOR ALTERNATIVE AND RENEWABLE ENERGY SOURCES & TECHNIQUES (I.S.A.R.E.S.T.)

IRAQI JOURNAL OF APPLIED PHYSICS

ISSN (Print): 1813-2065, ISSN (Online): 2309-1673, ISSN (Letters): 1999-656X

" INSTRUCTIONS TO AUTHORS "

CONTRIBUTIONS

Contributions to be published in this journal should be original research works, i.e., those not already published or submitted for publication elsewhere, individual papers or letters to editor.
Manuscripts should be submitted to the editor at the mailing address:
Iraqi Journal of Applied Physics, Editorial Board, P. O. Box 55259, Baghdad 12001, IRAQ
Website: www.iraqiphysicsjournal.com
Email: editor@iraqiphysicsjournal.com, editor_ijap@yahoo.co.uk

MANUSCRIPTS

Two hard copies with soft copy on a compact disc (CD) should be submitted to Editor in the following configuration:

- **One-column** Double-spaced one-side A4 size with 2.5 cm margins of all sides
- Times New Roman font (16pt bold for title, 14pt bold for names, 12pt bold for headings, 12pt regular for text)
- Letters should not exceed 10 pages, papers should not exceed 20 pages and reviews are up to author.
- Manuscripts presented in English only are accepted.
- English abstract not exceed 150 words
- 4 keywords (at least) should be maintained on (PACS preferred)
- Author(s) should express all quantities in SI units
- Equations should be written in equation form (*italic* and symbolic)
- Figures and Tables should be separated from text
- Figures and diagrams can be submitted in colors for assessment and they will be returned to authors after provide printable copies
- Charts should be indicated by the software used for
- Only original or high-resolution scanner photos are accepted
- For electronic submission, articles should be formatted with MS-Word software.

AUTHOR NAMES AND AFFILIATIONS

It is IJAP policy that all those who have participated significantly in the technical aspects of a paper be recognized as co-authors or cited in the acknowledgments. In the case of a paper with more than one author, correspondence concerning the paper will be sent to the first author unless staff is advised otherwise.
Author name should consist of first name, middle initial, last name. The author affiliation should consist of the following, as applicable, in the order noted:
- Company or college (with department name or company division), Postal address, City, state, zip code, Country name, contacting telephone, and e-mail

REFERENCES

The references should be brought at the end of the article, and numbered in the order of their appearance in the paper. The reference list should be cited in accordance with the following examples:
[1] X. Ning and M.R. Lovell, "On the Sliding Friction Characteristics of Unidirectional Continuous FRP Composites", *ASME J. Tribol.*, 124(1) (2002) 5-13.
[2] M. Barnes, "Stresses in Solenoids", *J. Appl. Phys.*, 48(5) (2001) 2000–2008.
[3] J. Jones, **"Contact Mechanics"**, Cambridge University Press (Cambridge, UK) (2000), Ch.6, p.56.
[4] Y. Lee, S.A. Korpela and R. Horne, "Structure of Multi-Cellular Natural Convection in a Tall Vertical Annulus", Proc. 7th International Heat Transfer Conference, U. Grigul et al., eds., Hemisphere (Washington DC), 2 (1982) 221–226.
[5] M. Hashish, "Waterjet Technology Development", High Pressure Technology, PVP-Vol. 406 (2000) 135-140.
[6] D.W. Watson, "Thermodynamic Analysis", ASME Paper No. 97-GT-288 (1997).
[7] C.Y. Tung, "Evaporative Heat Transfer in the Contact Line of a Mixture", Ph.D. thesis, Rensselaer Polytechnic Institute, Troy, NY (1982).

PROOFS

Authors will receive proofs of papers and are requested to return one corrected hard copy with a WORD copy on a compact disc (CD). New materials inserted in the original text without Editor permission may cause rejection of paper.

COPYRIGHT FORM

Author(s) will be asked to transfer copyrights of the article to the Journal soon after acceptance of it. This will ensure the widest possible dissemination of information.

OFFPRINTS

Authors will receive offprints free of charge and any additional reprints can be ordered.

SUBSCRIPTION AND ORDERS

Annual fees (4 issues per year) of subscription are:
50 US$ for individuals inside Iraq; **200** US$ for institutions inside Iraq;
100 US$ for individuals abroad; **300** US$ for institutions abroad.
Fees are reduced by 25% for I.S.A.R.E.S.T. members. Orders of issues can be submitted by contacting the editor-in-chief or editorial office at admin@iraqiphysicsjournal.com, or editor_ijap@yahoo.co.uk to maintain the address of issue delivery and payment way.

IRAQI JOURNAL OF APPLIED PHYSICS
Vol. 17, No. 3, July-September 2021, pp. 3-8

Effect of Operation Temperature on Characteristics of NiO-Doped Tellurium Oxide Thin Film Gas Sensors Prepared by Pulsed-Laser Deposition

Fatima A. Ahmed[1]
Michelle Battler[2]
Ayad H. Majeed[1]

[1] *Department of Physics, College of Science, Al-Muthanna University, Samawa, IRAQ*
[2] *School of Applied Physics, University of Bradford, Bradford, UK*

The influence of doping level of tellurium oxide films with different amounts of NiO additives (5, 10, 15 and 20%) on structural, optical, and electrical properties is investigated. The films were prepared by pulsed-laser deposition method. The Hall effect measurements show an increase in the conductivity with increase the NiO ratio and transfer the type of charge carriers from n to p-type with 20% NiO. The H_2S sensing properties are influenced by the NiO ratio in the TeO films as well as the operation temperature. The TeO sensor loaded with 10% NiO is extremely sensitive to H_2S and the best operation temperature is 50°C, and exhibits fast response speed of 7 s and recovery time of 20 s for trace level (10 ppm) H_2S gas detection.

Keywords: Tellurium oxide; Thin films; Pulsed-laser deposition; Gas sensing

1. Introduction

Tellurium-dioxide (TeO), also known as stannic oxide, is a widely used ceramic material [1]. It has a direct band-gap which width is equal to 3.6 eV [2] and high exciton binding energy of 130 meV, and excellent optical and electrical properties with outstanding chemical and physical stabilities in harsh environments [3,4]. Stoichiometric TeO is an insulator, small shifts from its perfect stoichiometry (i.e. TeO_{-x}, with x<1), or shallow doping (F or Sb) lead to n-type semi-conductive behavior of the material [5]. Its electrical conductance results from point defect such as oxygen vacancies and interstitial tellurium atoms, that acts as donor [6]. For this reason, TeO is grouped with a category of materials known as transparent conductive oxides (TCOs) which combines high electrical conductivity with optical transparency [7]. Due to their low fabrication cost, TeO thin films have a widely application such as gas sensor materials, low-emission glasses and heat mirrors, flat panel displays, touch panels, oxidation catalysts, flexible electronics, dye-sensitized solar cells (DSSCs), etc. [5-8]. TeO is considered one of the promising candidates for constructing the short wavelength optoelectronic devices, such as ultraviolet light emitting diodes (LEDs), laser diodes solar- and visible-blind photodetectors [4,9-11].

An increased concern over safety in civilian homes and industrial settings, much attention has been paid to the search for semiconductor gas sensor [12-17]. The detection and control of H_2S which is bad smelling and toxic gas is very important in laboratories and industrial areas where it is used as process gas or generated as a byproduct [16]. H_2S gas finds many applications in fields such as auto ventilation units, and medical field of dentistry [12,18].

The sensing properties of various semiconductor oxides, especially TeO-based materials, have been widely studied, which is the most preferred material for gas sensor application because of its enhanced ability to absorb oxygen on its surface and thus is highly sensitive towards many toxic and harmful gases [19]. The principle work of these sensors is a change in electrical conductance when exposure to the gas which is to be detected [20]. Desirable characteristics of a gas sensor are high sensitivity, selectivity, stability, fast response time, fast recovery time, and should be cost effective and reliable over long term [12,14,21].

The sensing properties of TeO gas sensors influence by many factors (intrinsic &extrinsic), the effective way to improve sensitivity and selectivity is modification of surface and bulk properties of tellurium oxide by doping [22]. It has been observes that the basic oxide additives promote the sensitivity and selectivity of TeO-based sensor to oxidation and reducing gases [23,24]. Nickel oxide (NiO) catalyst in TeO-based sensor is gaining a lot of importance for trace level detection of hydrogen sulfide (H_2S) gas [25]. In 1991, Maekawa et al. have presented the first report on enhanced sensitivity of TeO with NiO dopant to detect H_2S gas [26]. Subsequently several studies showed the high sensitivity and selectivity for NiO doped TeO sensors using, thin films of tellurium oxide doped with different amount of Cu dopant [27], Cu/TeO bilayers [28], TeO-NiO-TeO sandwich structure [29], thick and thin films of TeO doped with NiO [30]. NiO does not react with TeO, therefore p-n junctions formed between p-type NiO and n-type

TeO, which destroyed by formation CuS when exposure to H_2S gas [31,32].

In this work, NiO-doped TeO samples with different doping ratio were prepared by solid state reaction, which then used to fabricate film gas sensor by using pulsed laser deposition technique. The sensing characteristics of the NiO-TeO composite thin film with respect to H_2S gas were measured.

2. Experimental Details

Nickel oxide doped with different doping ratio (5, 10, 15, 20%) added to TeO powder and synthesized by solid state reaction by using NiO (99.9% Fluke) and TeO (99.5% ERAK). The two binary compounds mixed carefully for an hour and pressed at 5 ton to form a target (pellet shape with 13 mm diameter and 3 mm thickness), and then sintered in 950°C for two hours.

The NiO-doped TeO thin films have been prepared on glass and silicon substrates using pulsed laser deposition technique (PLD) with high quality using second harmonic generation (SHG) from a Nd:YAG Q-switched laser beam with a pulse width 10 ns, repetition frequency of 6 Hz and pulse energy of 400 mJ. The number of laser shots was 400 incident on the target surface with an angle of 45°. The deposition was carried out inside a vacuum chamber (10^{-2} mbar). Single crystal n-type silicon wafer substrates with phosphor doping, crystal orientation (111), thickness 508 μm and electrical resistivity of 1.5-4 Ω.cm. Square shape Si samples each of 10 mm^2 area were prepared. The films should be homogenous as possible to ensure good quality.

In order to measure the electrical properties, ohmic contacts are needed. It was obtained by evaporated Al wire of high purity under vacuum. The best condition for good ohmic contact was satisfied by a layer of 200 nm. The Hall effect measurements were carried out by using Ecopia 3000 HMS system.

Laser interferometer was used to measure the film thickness, which was in the range 200±20nm. The gas sensing properties were performed in the specially designed gas sensor test rig. The test rig was used with stainless steel cylindrical test chamber. The chamber had an inlet for the test gas to flow in and an air admittance valve. The changes in the resistance values of sensor which result from interaction with the target reducing H_2S gas with concentration 10 ppm were recorded using a data acquisition system consisting of multi-meter interfaced with a computer.

3. Result and Discussion

The type of charge carriers, conductivity, carrier concentration (n_H) and Hall mobility (μ_H), have been estimated from Hall measurements. Table (1) illustrates the main parameters estimated from Hall Effect measurements for TeO thin films deposited at room temperatures on glass substrates with different doping NiO ratio (5, 10, 15, 20%). It is clear from this table that pure and doped films with (5, 10, 15%) have a negative Hall coefficient (n-type),and change to p-type when the doping ratio increase to 20%.The conductivity increase with increasing the NiO ratio, its increase from $2.16x10^{-7}$ to $4.06x10^{-5}$ $(\Omega.cm)^{-1}$, and in general the Hall mobility (μ_H) also increase, while the carriers concentration (n_H) decrease with increasing doping ratio as shown in table (1).

Table (1) The electrical measurements of pure TeO and doped with different ratios of NiO films

Sample	Type	σ $x10^{-6}$ $(\Omega.cm)^{-1}$	n $x10^{11}$ (cm^{-3})	Mobility μ (cm/V.s)
Pure TeO	n-type	0.216	24.90	0.54
5% NiO	n-type	7.33	7.36	62.10
10% NiO	n-type	6.82	4.31	98.80
15% NiO	n- type	38.4	35.50	67.50
20% NiO	p-type	40.6	2.78	909.00

The gas sensitivity and response as well as recovery characteristics of pure TeO and NiO-doped TeO sensor elements were evaluated at room temperature, 50, 100 and 150 °C for H_2S gas to determine the optimum operating temperature of these sensors. Tellurium oxide films which prepared freshly adsorb oxygen atoms on the surface when it exposed to air. These oxygen atoms pick up the electrons from conduction band of tellurium oxide and transfer to O^- ions. So that the surface of tellurium oxide particle have negative charge, and there is a positive charge layer just below the surface particle due to depletion of electrons from donor atoms. When the TeO sensor exposed to reducing gas (H_2S) at room temperature and elevated temperature, the O^- ions on the surface react with the gas and release the electrons to the conduction band, as a result the depth of depletion layer decreases, this means the height of the potential barrier decreases and the resistance of sensor drops.

The sensitivity of NiO-doped TeO films to H_2S gas is increased due to the following mechanism. Due to an absence of interaction between TeO (n-type) and NiO (p-type) for sintered TeO:NiO films, the NiO grains are residing between TeO grains and forming a network of p-n junctions, that means a p-n junction forms at each interface between NiO and TeO grains. In an oxidizing atmosphere, a thick charge depletion layer is formed at the surface of TeO and this leads to a high resistance of the film in air. When the H_2S gas flows over the film, the NiO is converted into CuS which being metallic in character, the p-n junctions destroy and transformed to a metal/n-type semiconductor configuration. Since the work function of CuS is lower than that of TeO, the band is bending. This situation occurs because – at equilibrium – there is a flow of electrons from the material of lower work function (CuS) to that of higher work function (TeO). This results in the band bending downwards which facilitates the easy flow of electrons from CuS to TeO and vice versa (i.e., there is no potential barrier between them). The flow of electrons results in a decrease in the electrical

resistance. When the H_2S supply is turned off, CuS gets quickly oxidized to NiO, and the p-n junctions are restored [15].

Figure (1a) shows the dynamic resistance response of TeO sensor to 10 ppm H_2S gas at R.T, 50, 100, 150°C. The characteristic behavior of the resistance of the sensors decrease when expose to H_2S gas which is typical for n-type semiconductor oxide gas sensors. The relation between the resistance and the time of exposure to H_2S gas for TeO sensors doped with 5% of NiO is represented in Fig. (1b). It is obvious that the resistance of TeO film increases when the NiO ratio increases, this occur because nickel ions can be take either substitution or interstitial positions in the TeO lattice, since the radius of Cu (0.72Å) and Sn (0.71Å) is nearly equals, so that the Cu ions will occupy the substitution position and the reaction occurs as follows:

$$CuO + \frac{1}{2}O_2 \xrightarrow{SnO_2} Cu^{+2} + 2O + 2h \qquad (1)$$

This reaction means the substitution by Cu^{+2} causes increase "*h*" the hole concentration (oxygen vacancy), which lead to decrease in the free electron (increase the depletion layer width) and finally the resistance of TeO film increases. Also it is clear from this figure that the resistance of the TeO:NiO sensors decreases when its expose to H_2S gas.

The mechanism which explains the large decreases in resistance of TeO:NiO sensors on exposure to H_2S gas was suggested earlier [33,34].

Tellurium oxide is n-type semiconductors, when nickel oxide (p-type) adds as a dopant material, there is no chemical reaction occurs between them but the two semiconductors formed numerous p-n junctions causing very high resistance of films in air. The NiO particles converted to CuS semiconductor which is a metallic in nature by exposure to H_2S as shown by following reaction:

$$CuO + H_2S \longrightarrow CuS + H_2O \qquad (2)$$

As a result, the p-n junctions are destroyed because the band bends downward and no barrier exists between CuS which has lower work function than that of TeO. Thus the resistance of the sensors in H_2S is lower than that in air. After cease the flow of H_2S gas, the CuS oxidized by the oxygen in the chamber and converted back to NiO as follows [26]:

$$CuS + \frac{3}{2}O_2 \longrightarrow CuO + SO_2 \qquad (3)$$

The conversion of the CuS to NiO is slow at low temperatures, and the rate of oxidation increases with increasing temperature. This explains why the recovery rate of the sensor is faster at high temperatures [28].

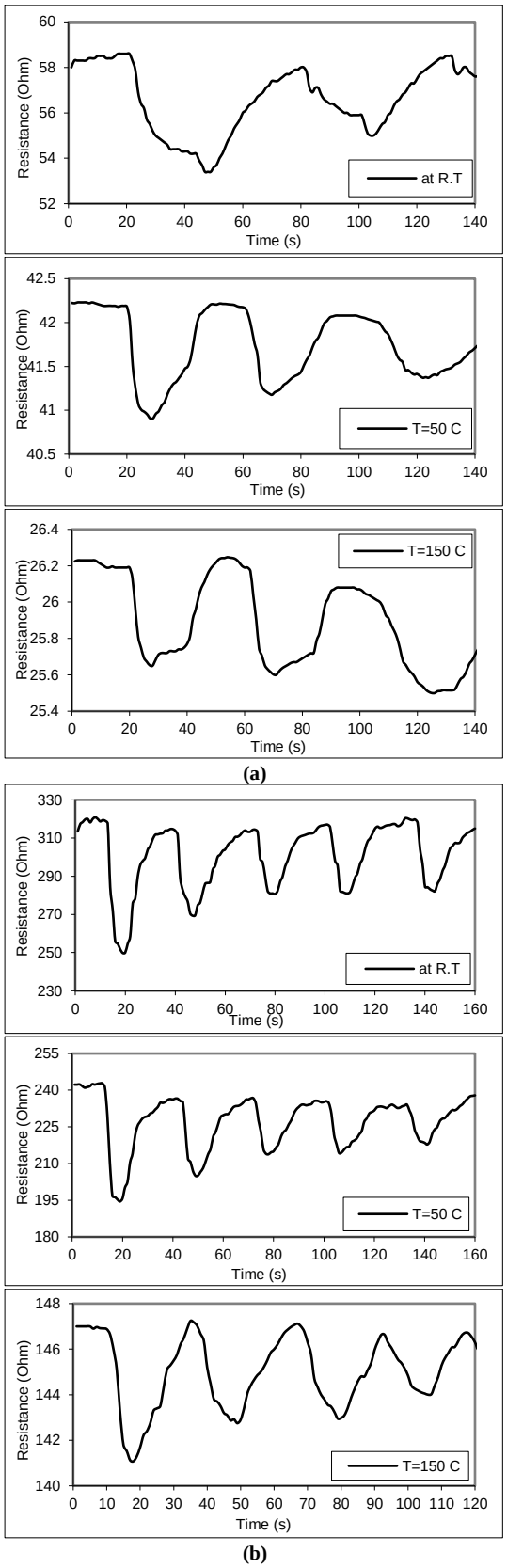

Fig. (1) The variation of resistance with time for (a) pure and (b) NiO-doped TeO films

The resistance response of each sensor structure was transformed into a sensitivity value which is one of the important parameters of gas sensors, the sensitivity of the metal oxide based materials, will

change with the factors influencing the surface reactions, such as chemical components, surface modification and microstructures of sensing layers, temperature and humidity [34-36]. The sensitivity (S) of the sensors can be defined as [14]:

$$S = \frac{R_a - R_g}{R_a} \quad (4)$$

where R_a and R_g are the resistance of the sensor in fresh air and in presence of the gas, respectively

The sensitivity of the sensors against 10 ppm H_2S at different temperatures are shown in Fig. (2). It is clear from this figure that the NiO additives improve the sensitivity to H_2S gas and the maximum sensitivity recorded for the two samples which doped with 10, and 15% NiO (nano-size grains). The best operation temperature is 50°C and the sensitivity decrease with increasing temperatures. CuS is converted to Cu_2S at temperature above 103°C and the resistance of Cu_2S is higher than that of CuS and this leads to reduce the sensitivity with increasing temperature.

Detection at such low temperatures is very important to be used in chemical industries and research laboratories [28]. The sensitivity of TeO:20% NiO sensor cannot be recorded because there is a disturbance behavior for this sensor. This attributed to that the high ratio of NiO (more than 15%) the transfer of NiO to CuS does not occur completely with 10 ppm H_2S, and the modulation in the depletion region is limited, resulting in a relatively higher value of R_g. Table (2) summarized the sensing parameters obtained for pure TeO and doped with different ratios of NiO sensors at different temperatures.

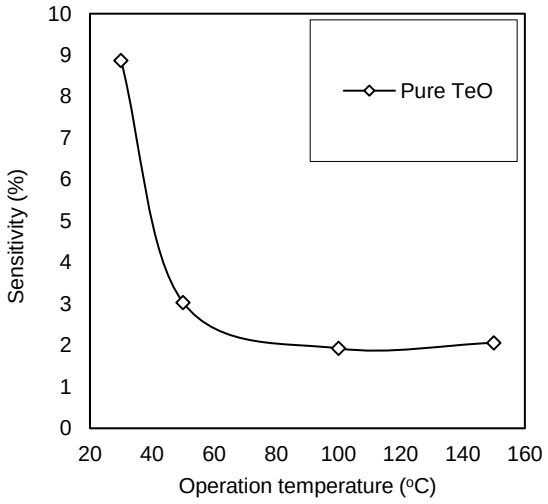

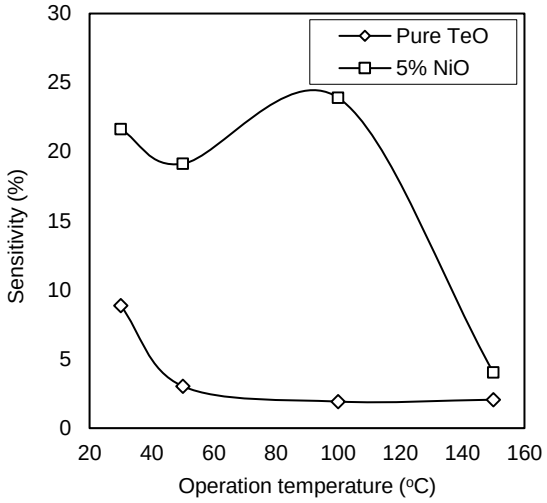

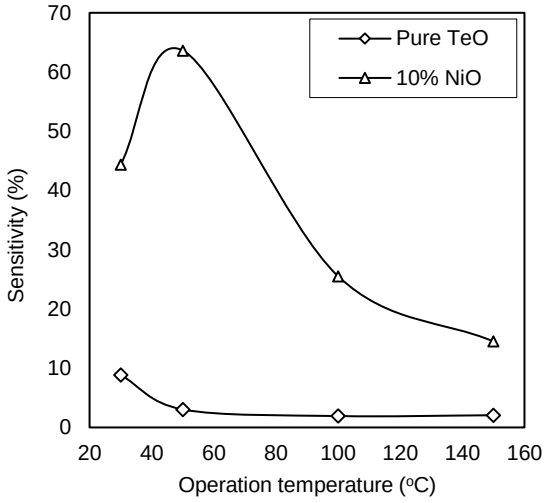

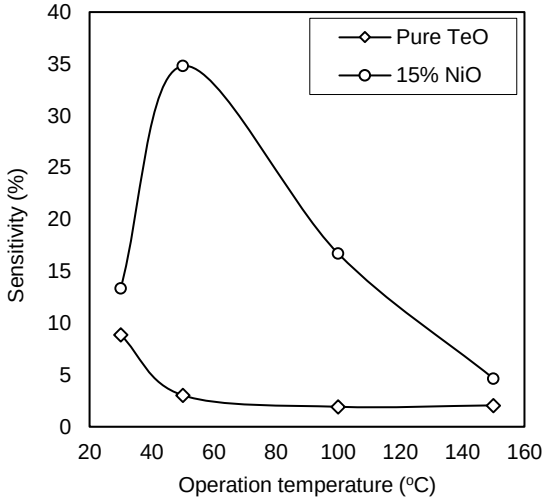

Fig. (2) (5) The variation sensitivity of the fabricated sensors with operation temperatures for different samples

Table (2) Gas sensing measurement data of pure TeO and doped with different ratios of NiO sensors at different temperatures

Materials	Temperature (°C)	Sensitivity (%)	Response time (s)	Recovery time (s)
Pure TeO	28	8.87	25.2	29
	50	3.03	8.1	20.7
	150	2.06	7.2	24.3
NiO-doped TeO (5%)	28	21.63	7.2	18.0
	50	19.63	7.0	19.8
	150	4.02	7.2	15.3
NiO-doped TeO (10%)	28	44.37	7.2	20.7
	50	63.63	7.0	16.2
	150	14.52	4.5	12.6
NiO-doped TeO (15%)	28	13.35	9.0	20.7
	50	34.80	7.2	29.7
	150	4.65	15.3	10.8

4. Conclusion

This study revealed the effect of NiO additives on structural, optical and electrical properties of TeO films deposited on glass substrates by pulsed laser deposition technique. All films are n-type, except film doped with 20% NiO has appositive hall coefficient. The NiO additives has a strong effect on the sensitivity of TeO films for trace level (10 ppm) H_2S gas detection and exhibits a fast response speed and quick recovery time. The sensors doped with 10 and 15% NiO (nano-sized grains) exhibit the maximum sensitivity at 50°C.

References

[1] A. Galdikas, A. Mironas and A. Šetkus, "Copper-doping level effect on sensitivity and selectivity of tin oxide thin-film gas sensor", Sensors & Actuators B, 26(1-3) (1995) 29-32.

[2] K.G. Godinho, A. Walsh and G.W. Watson, "Energetic and Electronic Structure Analysis of Intrinsic Defects in SnO_2", J. Phys. Chem., 113(1) (2009) 439-448.

[3] O.A. Hamadi, "Profiling of Antimony Diffusivity in Silicon Substrates using Laser-Induced Diffusion Technique", Iraqi J. Appl. Phys. Lett., 3(1) (2010) 23-26.

[4] S.S. Pan et al., "Optical properties of nitrogen-doped SnO_2 films: Effect of the electronegativity on refractive index and band gap", J. Appl. Phys., 103(9) (2008).

[5] D. Scorticati et al., "Optical and electrical properties of SnO_2 thin films after ultra-short pulsed laser annealing", Proc. SPIE 8826, Laser Material Processing for Solar Energy Devices II, 88260I (2013) doi: 10.1117/12.2023635.

[6] O.A. Hamadi, "Characteristics of CdO-Si Heterostructure Produced by Plasma-Induced Bonding Technique", Proc. IMechE, Part L, J. Mater.: Design and Applications, 222(1) (2008) 65-71.

[7] Y. Shimizu and M. Egashira, "Basic aspects and challenges of semiconductor gas sensors", Mater. Res. Bull., 24(6) (1998) 18-24.

[8] O.A. Hammadi and N.E. Naji, "Electrical and Spectral Characterization of CdS/Si Heterojunction Prepared by Plasma-Induced Bonding", Opt. Quant. Electron., 48(8) (2016) 375.

[9] S. Singh et al., "Synthesis and characterization of CuO–SnO_2 nanocomposite and its application as liquefied petroleum gas sensor", Mater. Sci. in Semicond. Process., 18 (February 2014) 88-96.

[10] O.A. Hammadi, "Characteristics of Heat-Annealed Silicon Homojunction Infrared Photodetector Fabricated by Plasma-Assisted Technique", Phot. Sen., 6(4) (2016) 345-350.

[11] O.A. Hammadi, M.K. Khalaf, F.J. Kadhim, "Fabrication and Characterization of UV Photodetectors Based on Silicon Nitride Nanostructures Prepared by Magnetron Sputtering", Proc. IMechE, Part N, J. Nanoeng. Nanosys., 230(1) (2016) 32-36.

[12] R.G. Gordon, "Criteria for choosing transparent conductors", MRS Bulletin, 25(8) (2000) 52-57.

[13] B. Zhang et al., "The FTIR studies on the structural and electrical properties of SnO_2:F films as a function of hydrofluoric acid concentration", Opt. Adv. Mater., 4(8) (2010) 1158-1162.

[14] J.K. Srivastava, A. Gupta and A.A. Bhaskar, "Sensing Behavior Of CuO-Doped SnO_2 Thick Film Sensor For H_2S Detection", Int. J. Sci. Technol. Res., 3(5) (2014) 266-272.

[15] P.S. Pa, "Nanoscale Removal Fabrication for Touch Sensing Materials via Two Groups Mated Cylinder-Tool", Adv. Sci. Lett. 20(8) (2014) 95-98.

[16] J.C. Sohn et al., "H_2S Gas Sensing Properties of SnO_2:CuO Thin Film Sensors Prepared by E-beam Evaporation", Trans. Electr. Electron. Mater., 10(4) (2009) 135-139.

[17] O.A. Hamadi, B.A.M. Bader and A.K. Yousif, "Electrical Characteristics of Silicon p-n Junction Solar Cells Produced by Plasma-Assisted Matrix Etching Technique", Eng. Technol. J., 28 (2008).

[18] R.K. Sonker et al., "Nanocatalyst (Pt, Ag and CuO) Doped SnO_2 Thin Film Based Sensors for Low Temperature Detection of NO_2 Gas", Adv. Sci. Lett., 20(7-9) (2014) 1374-1377.

[19] J. Liu et al., "H_2S Detection Sensing Characteristic of CuO/SnO_2 Sensor", Sensors, 3(5) (2003) 110-118.

[20] A. Sharma, M. Tomar and V. Gupta, "Improved response characteristics of SnO_2 film based NO_2 gas sensor with nanoscaled metal oxide catalysts", Proc. of the 14th Int. Meet. on Chem. Sensors, 2012 (IMCS 2012), 702-705, doi: 10.5162/IMCS2012/8.3.4.

[21] B.C. Yadav et al., "Fabrication and characterization of nanostructured indium tin oxide film and its application as humidity and gas sensors", J. Mater. Sci.: Mater. In Electron., 27(5) (2016) 4172-4179.

[22] A. Galdikas, A. Mironas and A. Setkus, "Copper-doping level effect on sensitivity and selectivity of tin oxide thin-film gas sensor", Sensors & Actuators B, 26(1-3) (1995) 29-32.
[23] S. Matsushima et al., "Role of additives on alcohol sensing by semiconductor gas sensor", Chem. Lett., 18(5) (1989) 845-848.
[24] O.A. Hamadi, "Characterization of SiC/Si Heterojunction Fabricated by Plasma-Induced Growth of Nanostructured Silicon Carbide Layer on Silicon Surface", Iraqi J. Appl. Phys., 12(2) (2016) 9-13.
[25] A. Chowdhuri et al., "Response speed of SnO_2-based H_2S gas sensors with CuO nanoparticles", Appl. Phys. Lett., 84(7) (2004) 1180-1182.
[26] T. Maekawa et al., "Sensing behavior of CuO loaded SnO_2 element for H_2S detection", Chem. Lett., 20(4) (1991) 575-578.
[27] L. Jianping et al., "H_2S sensing properties of the SnO_2-based thin films", Sensors and Actuators B, 65(1-3) (2000) 111-113.
[28] W. Yuanda et al., "Thin film sensor of SnO_2-CuO-SnO_2 sandwich structure to H_2S", Sensors and Actuators B, 79(2-3) (2001) 187-191.
[29] A. Khanna, R. Kumar and S.S. Bhatti, "CuO-doped SnO_2 thin films as hydrogen sulfide gas sensor", Appl. Phys. Lett., 82(24) (2003) 4388-4390.
[30] X. Kong and Y. Li, "High sensitivity of CuO modified SnO_2 nanoribbons to H_2S at room temperature", Sensors and Actuators B, 105(2) (2005) 449-453.
[31] X. Xue et al., "Synthesis and H_2S Sensing Properties of CuO-SnO_2 Core/Shell PN-Junction Nanorods", J. Phys. Chem. C, 112(32) (2008) 12157–12160.
[32] G.S. Devi, S. Manorama and V.J. Rao, "High sensitivity and selectivity of an SnO_2 to H_2S at around 100°C", Sensors and Actuators B, 28(1) (1995) 31-37.
[33] A. Chowdhuri et al., "H_2S gas sensing mechanism of SnO_2 films with ultrathin CuO dotted islands", J. Appl. Phys., 92(4) (2002) 2172.
[34] C. Wang et al., "Metal Oxide Gas Sensors: Sensitivity and Influencing Factors", Sensors, 10(3) (2010) 2088-2106.
[35] O.A. Hammadi, M.K. Khalaf, F.J. Kadhim, "Fabrication of UV Photodetector from NiO Nanoparticles Deposited on Silicon Substrate by CFUBDM Sputtering Technique", Opt. Quantum Electron., 47(12) (2015) 3805-3813.
[36] F.J. Kadhim and A.A. Anber, "Fabrication of nanostructured silicon nitride thin film gas sensors by reactive direct current magnetron sputtering", Proc. IMechE, Part N, J. Nanoeng. Nanosys., 231(4) (2018) 173-178.

IRAQI JOURNAL OF APPLIED PHYSICS
Vol. 17, No. 4, October-December 2021, pp. 9-14

Photocatalytic Performance of Mixed and Single Phases of Titanium Dioxide Nanoparticles on Growth of Fusarium Oxysporum Fungal

Maryam A. Nima
Firas J. Kadhim

Department of Physics, College of Science, University of Baghdad, Baghdad, IRAQ

In this work, the photocatalytic activity was considered to inactivate Fusarium oxysporum fungal under UV radiation exposure using highly-pure TiO_2 nanoparticles. These nanoparticles were extracted from thin film samples prepared by dc reactive magnetron sputtering system. The mixed-phase (anatase+rutile) films were prepared using two different gas mixing ratios and different deposition times (3, 3.30 and 4 hours). Accordingly, the weight fractions of rutile in mixed-phase were 40, 46 and 50%, respectively. The single phase (anatase) was produced without any heat treatment using specific mixing ratio of 50:50. The structural and spectroscopic characteristics of the prepared nanoparticles were determined and analyzed. At weight fraction of 40% of mixed-phase TiO_2, the best antifungal activity was achieved.

Keywords: Titanium dioxide; Photocatalytic activity; Nanoparticles; Antifungal
Received: 15 September 2021; **Revised:** 05 October 2021; **Accepted:** 12 October 2021

1. Introduction

Nanostructured materials have garnered considerable interest as catalysts and in another applications, due to their distinctive structural characteristics. The essential metal oxides such as titanium dioxide (TiO_2) have received a lot of attention, due to its alchemical stability, optical, physical, and electrical characteristics. The photocatalytic characteristics be applied to the removal of contaminants from both water and air in a variety of environmental applications including water purification [1,2]. Titanium dioxide is exists as anatase, rutile, and brookite. Although rutile is the most widespread and stable form of titanium dioxide, anatase is preferred for its high photocatalytic activity [3]. The mixed-phase (anatase/rutile) is widely used much more than the anatase or rutile phase have higher photocatalytic effectiveness than the single phase (anatase) or mixed phase (rutile) that is due to a synergistic impact between the two phases [4,5].

Titanium dioxide have a wide spectrum of antifungal activities microorganisms of fungal. Additionally, recent research has demonstrated that titanium dioxide cannot only destroy a complex cellular assembly with significant consequences for pathogenicity (fungal) as concentration rise, but it also has the ability to prevent the formation of fungus at decrease concentrations [6-8].

The direct current (DC) reactive magnetron sputtering method has that rely on momentum exchange to release atoms from a solid or liquid source. For decades, sputter deposition has been used to deposit thin films as a flexible, reliable, and successful approach. Operating factors such as total gas pressure, distance between electrodes, gas mixing ratio, electrical discharge power, substrate temperature, and sputtering time can all affect the properties of titanium dioxide films [9-12].

The anti-fungal activity of two structural phases of TiO_2 nanopowder is studied and compared in this work depending on the growth of fungal (Fusarium oxysporum) as a function of TiO_2 concentration.

2. Experimental Part

Titanium dioxide thin films were deposited on glass substrates using a direct current, closed-field unbalanced reactive magnetron sputtering system. Highly-pure Ti (99.99%) target was sputtered in the presence of oxygen gas as a reactive gas and argon gas as a discharge gas with a constant inter-electrode distance of 4 cm. Three various deposition times (3, 3:5, and 4 hours) and three various mixing ratios of $Ar:O_2$ gases (50:50, 67:33, and 80:20) were used to prepare the film samples. The conditions of preparation in detail can be found elsewhere [13,14]. Nanopowders were extracted from thin film samples (Fig. 1) using conjunctional freezing-assisted ultrasonic extraction method [15,16].

The fungal Fusarium oxysporum was chosen and prepared for the experiments of photocatalytic activity. To create the medium for fungal growth, 39 g of potato dextrose agar (PDA) was dissolved in 1 liter of distilled water. After 10 minutes of heating to fully melt, the medium was sanitized by autoclaving at 15 lbs., pressure (121°C), cool to 47°C, mix well then the medium was dispensed into sterile Petri dishes and stored in the fridge overnight. A small

amount of the Fusarium oxysporum fungal was applied equally on the surface of the PDA.

Fig. (1) Photograph of TiO_2 nanopowder extracted from the thin film samples prepared in this work

An ultrasonic bath was used to dissolve TiO_2 nanopowders in deionized water, which was then homogenized using a vortex mixer. A small amount of TiO_2 nanoparticles was spread equally over the surface of PDA with deionized water as a control and the dishes were then exposed to UV radiation (200-400nm) for 60 minutes. The UV light source was placed at 10 cm away from the Petri dish. Finally, the cells were cultured at 37°C for 24 hours and then inspected for the creation of outgrowth inhibitory zones. Figure (2) shows the fungal (Fusarium oxysporum) before performing the experiments of photocatalytic activity.

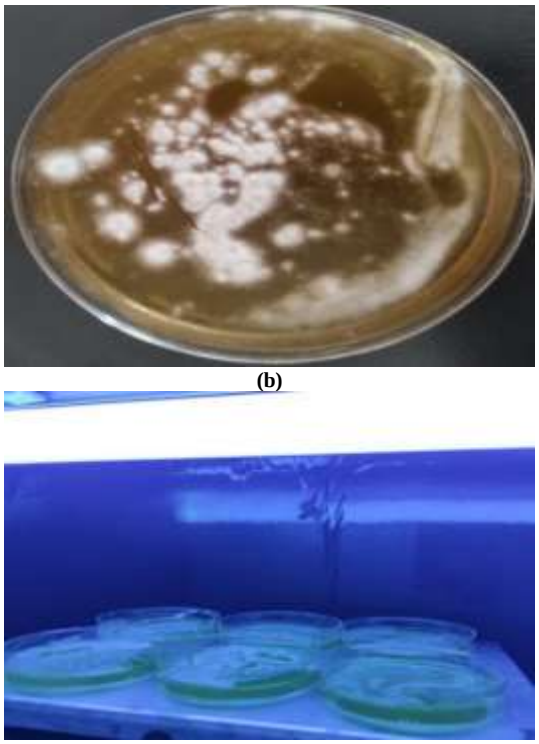

(b)

Fig. (2) Photographs of growth fungal (Fusarium oxysporum) (a) and the arrangement of photocatalytic activity measurement (b)

3. Results, and Discussion

The x-ray diffraction patterns of TiO_2 (mixed- and single-phase) thin films prepared in this work are shown in Fig. (3). Both phases are identified (rutile; R and anatase; A) [17]. The weight fraction (f) of rutile phase in the prepared sample can be determined by following equation [18]:

$$f = \frac{1}{1+0.88\frac{I_A}{I_R}} \quad (1)$$

where f is the weight fraction of rutile (R) in mixed-phase (A+R) and I_A/I_R is the ratio of anatase to rutile phase intensity as determined by x-ray intensities

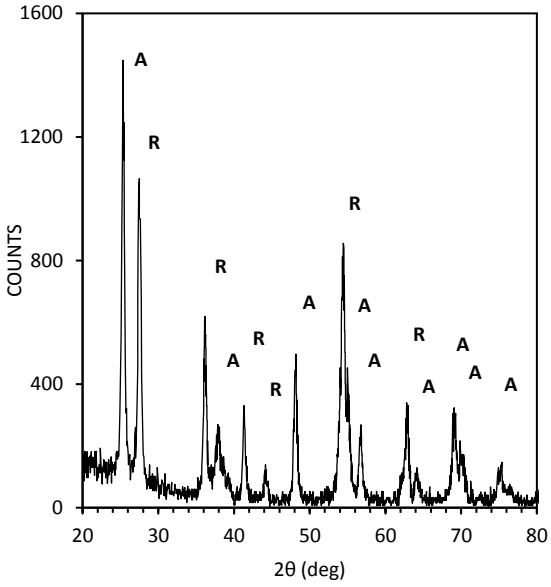

(a)

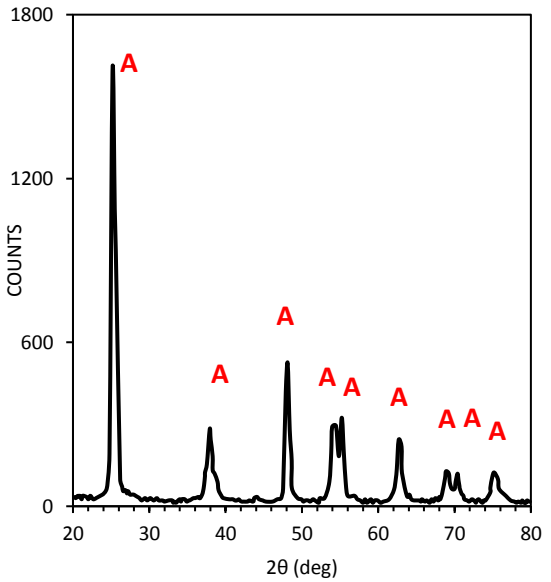

(b)

Fig. (3) XRD patterns of mixed-phase TiO_2 sample (a) and single-phase TiO_2 sample (b) prepared using gas mixing ratio of 50:50 and deposition time 3 hours

For samples produced after deposition times of 3, 3:30, and 4 hours, the percentage quantities of rutile in mixed-phase (anatase-rutile) samples were 40, 46

and 50%, respectively. The XRD pattern of the TiO_2 sample of anatase phase only is shown in Fig. (3b), where no peaks belonging to the rutile phase were observed.

The Fourier-transform infrared (FTIR) spectrum of prepared titanium dioxide nanopowder in the range 400-4000 cm^{-1} is shown in Fig. (4). This spectrum was recorded using Shimadzu 8400S FTIR instrument. The IR bands at 3464 and 1639 cm^{-1} are allocated to the stretching and bending vibrations of the OH group in water molecules [19,20]. At roughly 486 and 622 cm^{-1}, the band associated with Ti-O stretching vibrations was found, whereas the peak at 420 cm^{-1} is attributed to Ti-O-Ti bonds in the TiO_2 molecule [21]. As a result, the samples may be classified as highly-pure with no peaks ascribed to contaminations.

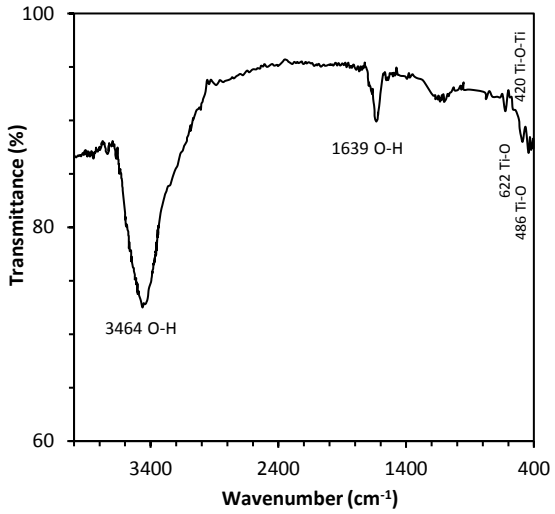

Fig. (4) FTIR spectrum of mixed-phase TiO_2 thin film prepared after deposition time of 3 hours

Scanning electron microscopy (SEM) was utilized to examine the surface profile and grain size of the prepared thin film samples, as illustrated in Fig. (5). Average particle size was 10.5 nm for the mixed-phase sample and 10.2 nm for the single-phase sample. The SEM image of the mixed-phase sample (Fig. 5a) reveals that the particles had nearly homogeneous distribution, which is one of the major advantages of the dc magnetron sputtering technique used for synthesis of nanostructures. On the other hand, the SEM image of the single-phase sample (Fig. 5b) clearly shows the aggregation and formation of large particles as only single phase is formed with a dominant crystal plane and some other planes.

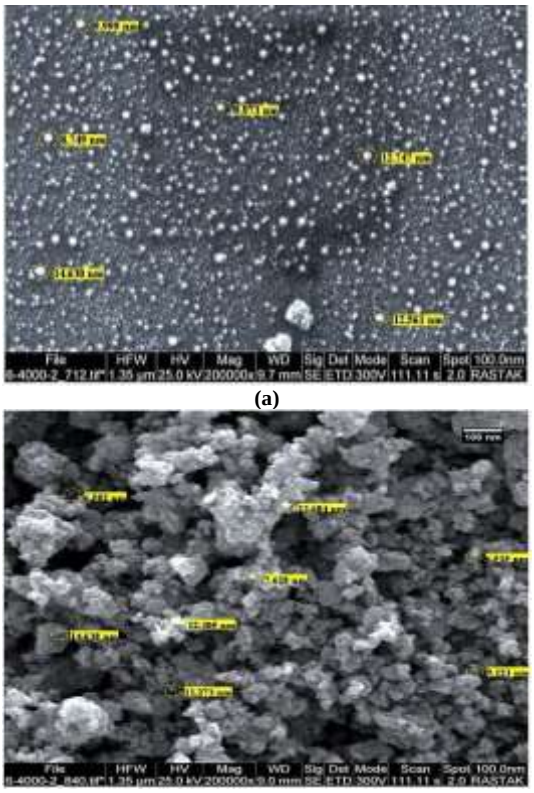

(a) **(b)**

Fig. (5) SEM images of mixed-phase TiO_2 (a) and single-phase TiO_2 samples prepared after deposition time of 3 hours

Figure (6) shows the EDX spectra of the same TiO_2 samples. The presence of Ti and O is indicated by the weight ratio (Ti:O) of 37.73:61.25 for the mixed-phase sample and 60.37:37.59 for the single-phase sample. These results may highlight the structural purity of the prepared samples as no traces belonging to other elements than Ti and O were observed. The peak of Al in these spectra is originated from the material of sample holder.

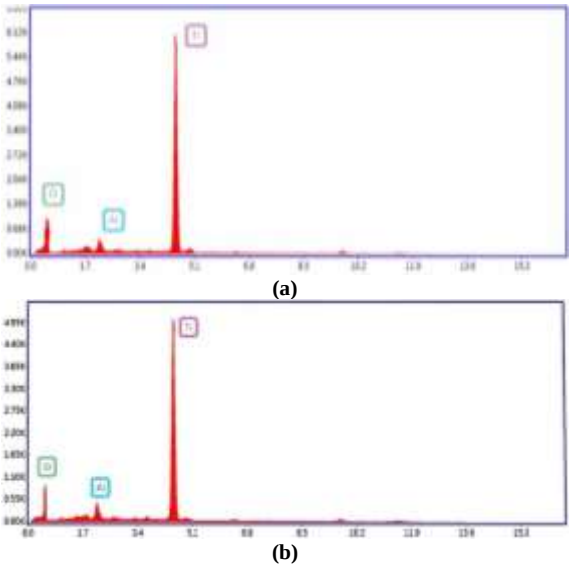

(a) **(b)**

Fig. (6) EDX spectra of mixed-phase TiO_2 (a) and single-phase TiO_2 samples prepared after deposition time of 3 hours

The UV-visible, spectroscopy was used to record and investigate the absorption spectra of both mixed-phase and single-phase TiO_2 film, samples in the spectral region,300-800 nm as shown in Fig. (7). The mixed-phase samples prepared after different deposition times showed identical behaviors as the absorbance is relatively high in the UV region (<380nm) and reasonably decreasing in the visible region. Obviously, the sample of higher thickness shows higher absorbance due to the higher optical density. The single-phase sample showed lower absorbance with respect to the mixed-phase samples in the same wavelength range (<380nm) as well as lower absorbance in the visible region. This is attributed to the contributions of both phases (rutile and anatase) in the mixed-phase sample while the only contribution in the single-phase sample is due to anatase phase.

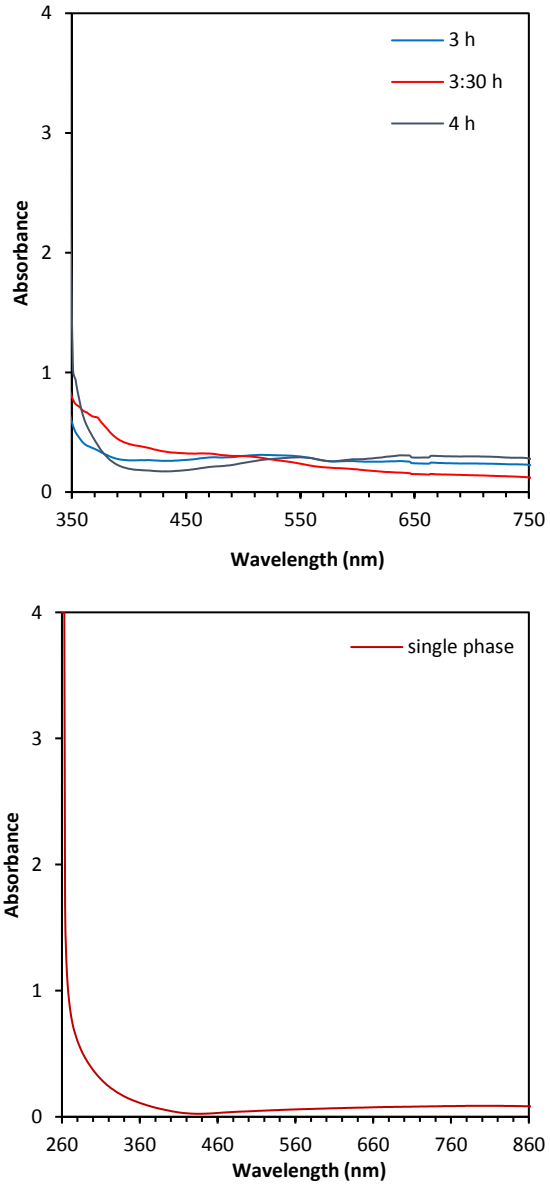

Fig. (7) Absorption spectra of mixed-phase sample (upper) and single-phase sample (lower)

The absorption characteristics of the TiO_2 nanopowders used for anti-fungal applications are very important as they determine how far the incident radiation (e.g., solar radiation) is invested to induce the photocatalytic activity of these nanopowders [22]. Therefore, the assessment of which samples are better can be based on the experimental test of the prepared samples to inactivate the fungal under test.

The energy band gap (E_g) can be calculated using Eq. (2) and extrapolation of the curve to intersect the photon energy ($h\nu$) axis, as shown in Fig. (8) to be 3.41eV for mixed-phase sample and 3.23 eV for single-phase sample [23,24] as

$$(\alpha h\nu)^r = A\,(h\nu - E_g) \qquad (2)$$

where α is coefficient of linear absorption, h is Planck's constant, ν is incident photon frequency, A is constant, and r is a constant determined by the type of optical transition. Here, r was chosen to be 0.5 to indicate that direct transitions are allowed [25]

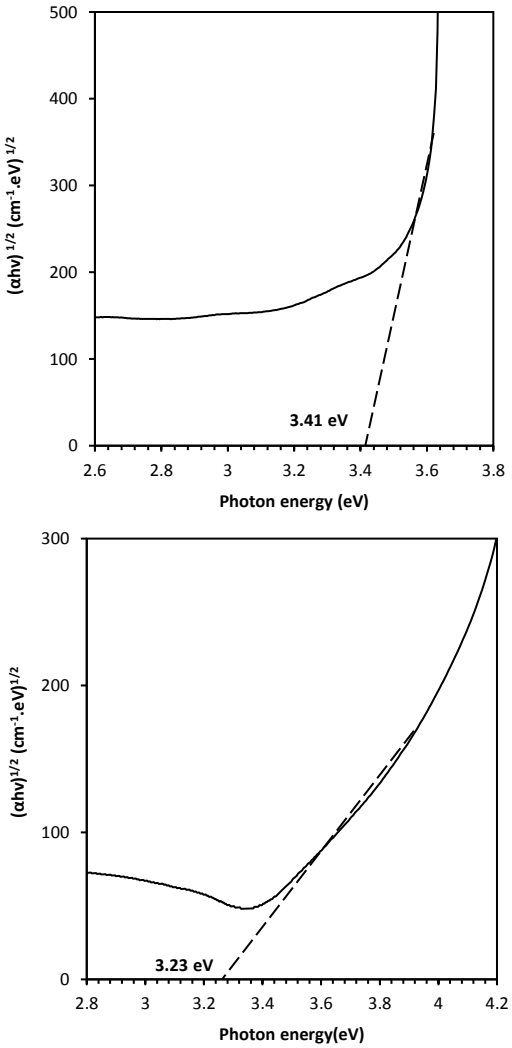

Fig. (8) Determination of energy band gap of mixed-phase sample (upper) and single-phase sample (lower)

The antifungal activity of TiO_2 nanoparticles at a concentration of (1g) against Fusarium oxysporum before, and after photocatalytic,treatment is depicted

in Fig. (9). The activity of TiO_2 nanoparticles is associated with the light-induced free radical production which results in peroxidation when the radical contacts with the fungal cell membrane. The highly-active oxygen has the ability to oxidize organic molecules that results in inactivation and then decomposition of the fungal.

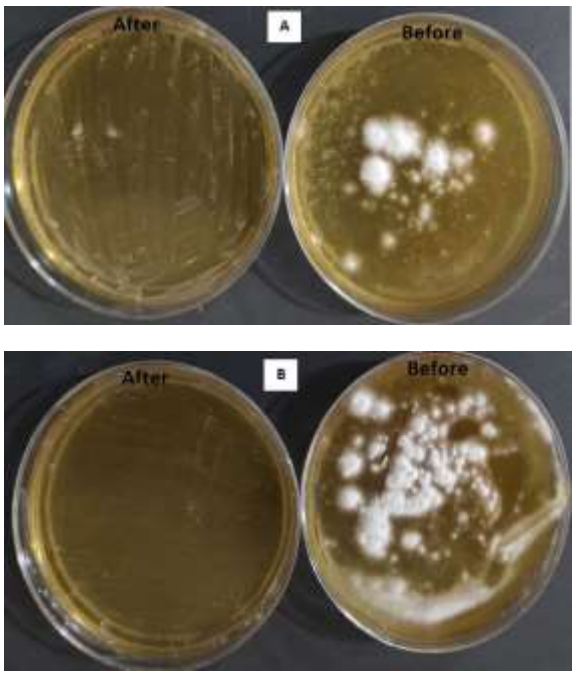

Fig. (9) Anti-fungal activity of TiO_2 nanoparticles (a) mixed-phase and (b) single-phase samples at concentration of 1g against F. oxysporum with 60 minutes of UV radiation exposure

4. Conclusion

In this study, high-quality mixed-phase nanostructured TiO_2 thin films were prepared using dc reactive magnetron sputtering technique. It was found that the weight fraction of the rutile phase in the mixed-phase samples depends on the deposition time, after which the sample was prepared. The sample with 40% rutile content exhibited the best photocatalytic activity. Synthesis of single-phase (anatase) TiO_2 samples was achieved without any heat treatment. It was also found that both types of TiO_2 samples (mixed- and single-phase) exhibit significant antifungal activity.

References

[1] S. Pavasupree et al., "Hydrothermal synthesis, characterization, photocatalytic activity and dye-sensitized solar cell performance of mesoporous anatase TiO_2 nanopowders", Mat. Res. Bull., 43 (2008) 149-157.
[2] R.A.H. Hassan and F.T. Ibrahim, "Preparation and Characterization of Anatase Titanium Dioxide Nanostructures as Smart and Self-Cleaned Surfaces", Iraqi J. Appl. Phys., 16(4) (2020) 13-18.
[3] D.P. Macwan, P.N. Dave and S. Chaturvedi, "A review on nano-TiO_2 sol-gel type syntheses and its applications", J. Mater. Sci., 46(11) (2011) 3669-3686.
[4] F.J. Al-Maliki1, O.A. Hammadi and E.A. Al-Oubidy, "Optimization of Rutile/Anatase Ratio in Titanium Dioxide Nanostructures prepared by DC Magnetron Sputtering Technique", Iraqi J. Sci., 60(Special Issue) (2019) 91-98.
[5] F. Haghighi et al., "Antifungal Activity of TiO_2 nanoparticles and EDTA on Candida albicans Biofilms", Infec. Epidem. Med., 1(1) (2013).
[6] F.J. Al-Maliki, O.A. Hammadi, B.T. Chiad and E.A. Al-Oubidy, "Enhanced photocatalytic activity of Ag-doped TiO_2 nanoparticles synthesized by DC Reactive Magnetron Co-Sputtering Technique", Opt. Quantum Electron., 52 (2020) 188.
[7] M.V. Berridge et al., "The Biochemical and Cellular Basis of Cell Proliferation Assays That Use Tetrazolium Salts", Biochemica, 4 (1996) 14-19.
[8] W.M. Dunne, "Bacterial adhesion: seen any good biofilms lately", Clin. Microbiol. Rev., 15 (2002) 155-166.
[9] A.A. Hussain and H.S. Wahab, "Synthesis and spectroscopic characterization of anatase TiO_2 nanoparticles", Int. J. Nanotech. Nanosci., 2 (2014) 1-6.
[10] W.B. Mi, E.Y. Jiang and H.L. Bai, "Structure, magnetic and optical properties of poly-crystalline Co-doped TiO_2 films", J. Magn. Magn. Mater., 321(16) (2009) 2472-2476.
[11] S.H. Faisal and M.A. Hameed, "Heterojunction Solar Cell Based on Highly-Pure Nanopowders Prepared by DC Reactive Magnetron Sputtering", Iraqi J. Appl. Phys., 16(3) (2020) 27-32.
[12] E.A. Al-Oubidy and F.J. Al-Maliki, "Effect of Gas Mixing Ratio on Energy Band Gap of Mixed-Phase Titanium Dioxide Nanostructures Prepared by Reactive Magnetron Sputtering Technique", Iraqi J. Appl. Phys., 14(4) (2018) 19-23.
[13] F.J. Al-Maliki and E.A. Al-Oubidy, "Effect of gas mixing ratio on structural characteristics of titanium dioxide nanostructures synthesized by DC reactive magnetron sputtering", Physica B: Cond. Matter, 555 (2019) 18-20.
[14] O.A. Hammadi, M.K. Khalaf, F.J. Kadhim and B.T. Chiad, "Operation Characteristics of a Closed-Field Unbalanced Dual-Magnetrons Plasma Sputtering System", Bulg. J. Phys., 41(1) (2014) 24-33.
[15] O.A. Hammadi, "Production of Nanopowders from Physical Vapor Deposited Films on Nonmetallic Substrates by Conjunctional Freezing-Assisted Ultrasonic Extraction Method", Proc. IMechE, Part N, J. Nanomater. Nanoeng. Nanosys., 232(4) (2018) 135-140.
[16] O.A. Hammadi, "Effects of Extraction Parameters on Particle Size of Titanium Dioxide Nanopowders Prepared by Physical Vapor Deposition Technique", Plasmonics, 15(6) (2020) 1747-1754.

[17] M. Ladd and R. Palmer, **"Structure Determination by X-Ray Crystallography"**, 5th ed., Springer (NY, 2013), 568.
[18] S.F. Bertram, **"Handbook of X-rays"**, ed. E.F. Kaelbe, McGraw-Hill (NY, 1976), 817.
[19] F.J. Al-Maliki and N.H. Al-Lamey, "Synthesis of Tb-doped titanium dioxide nanostructures by sol–gel method for environmental photocatalysis applications", J. Sol-Gel Sci. Technol., 81(1) (2016) 276-283.
[20] J.G. Yu et al., "Effects of pH on the microstructures and photocatalytic activity of mesoporous nanocrystalline titania powders prepared via hydrothermal method", J. Mol. Catal. A: Chem., 258(1-2) (2006) 104-112.
[21] K. Balachandran, R. Venckatesh and R. Sivaraj, "Synthesis of nanoTiO_2-SiO_2 composite using sol-gel method: effect of size, surface morphology and thermal stability", Int. J. Eng. Sci. Technol., 2 (2010) 3695-3700.
[22] O.A. Hammadi, F.J. Kadhim and E.A. Al-Oubidy, "Photocatalytic Activity of Nitrogen-Doped Titanium Dioxide Nanostructures Synthesized by DC Reactive Magnetron Sputtering Technique", Nonl. Opt. Quantum Opt., 51(1-2) (2019) 67-78.
[23] A. Zachariah et al., "Synergistic Effect in Photocatalysis As Observed for Mixed-Phase Nanocrystalline Titania Processed via Sol-Gel Solvent Mixing and Calcination", J. Phys. Chem. C, 112 (2008) 11345-11356.
[24] Y. Zhao et al., "Synthesis and optical properties of TiO_2 nanoparticles", Mater. Lett., 61 (2007) 79-83.
[25] E.A. Al-Oubidy and F.J. Kadhim, "Photocatalytic activity of anatase titanium dioxide nanostructures prepared by reactive magnetron sputtering technique", Opt. Quant. Electron., 51(1) (2019) 23.

IRAQI JOURNAL OF APPLIED PHYSICS
Vol. 17, No. 4, October-December 2021, pp. 15-18

Effect of Thermal Annealing on Photoluminescence Characteristics of Titanium Dioxide Thin Films Doped with Copper Oxide by Pulsed-Laser Deposition

Ali Rasoli
Ayda Faeghinia
Amir Taghawi

Department of Materials Engineering, Faculty of Mechanical Engineering, University of Tabriz, Tabriz, IRAN

In this work, titanium dioxide thin films were deposited on glass substrates and doped with copper oxide at different concentrations (0.0, 0.05, 0.1, 0.15 and 0.2 wt.%) by pulsed-laser deposition technique followed by thermal annealing at different temperatures (423 and 523 K) to study the effects of annealing temperature on their photoluminescence characteristics. The results of photoluminescence emission showed that there are two peaks positioned at 320 and 400 nm for predominated peak and at 620 and 680 nm for the small peaks. It was found that the energy band gap of the prepared samples was decreasing with increasing the content of copper oxide dopants in titanium dioxide thin films regardless the value of annealing temperature.

Keywords: Titanium dioxide; Copper oxide; Photoluminescence; Thermal annealing

1. Introduction

In the processes of heterogeneous catalysis, surface area plays the main role. In the processes of photocatalysis, the redox potential of charge carriers and the selectivity of the catalyst surface are important [1,2]. Recently, nanostructured materials have been considered for these purposes. The most popular of these is titanium dioxide [3]. TiO_2 is a semiconductor whose photocatalytic properties deteriorate under visible light due to its wide band gap [4]. It is known that doping increases the photocatalytic activity of TiO_2 upon irradiation with visible light. The nature of the dopant ion also affects this activity since the dopants can be interstitial, substitutional, or both in the case of incorporation [5]. Different locations have a different effect on the properties of titanium dioxide [6]. A comparison of the effectiveness of photocatalytic decomposition or synthesis of organic compounds is difficult since doping is carried out using different methods (sol–gel, solid reaction/mechanical activation, chemical vapor deposition, *etc.*), in which various precursors of metal ions are used [6-8]. This can also affect the photocatalytic activity of the resulting samples.

Titanium dioxide has been one of the most extensively studied oxides because of its remarkable optical and electronic properties [9-11]. Titanium dioxide films have attracted attention for use in fabricating capacitors in microelectronics devices due to their unusually high dielectric constant [12]. Titanium dioxide thin films have high band energy gap of 3.2-3.29 eV and 3.69-3.78 eV for allowed and forbidden direct transition, respectively [13]. Crystalline titanium dioxide film exists in three phases: rutile (tetragonal with a=0.4594 nm, c=0.2958 nm), anatase (tetragonal with a=0.3785 nm, c=0.9514 nm), and brookite (orthorhombic with a=0.9184 nm, b=0.5447 nm, c=0.5145 nm). Amongst the three phases, the rutile is the most stable and its formation depends on the starting material, deposition method and treatment temperature. In particular, titanium dioxide thin films can transform from amorphous phase into crystalline anatase and from anatase into rutile by changing temperature [14,15]. Rutile is usually the dominant phase in titanium dioxide films, but in some recent work, anatase-rich films have been synthesized. Many deposition methods can be used to prepare titanium oxides film: thermal [16] or anodic [17] oxidation of titanium, electron beam evaporation [18], chemical vapor deposition (CVD) [19], plasma-enhanced chemical vapor deposition PE-CVD [20], plasma-induced bonding (PIB) [21], sol-gel method [22,23], reactive sputtering methods [24-27] and pulsed-laser deposition (PLD) technique [28,29], which was first used by smith and Turner in 1965 to prepare semiconductor and dielectric thin films and was established due to the work of Dijkkamp and coworkers [30] on high-temperature superconductors in 1987.

Copper oxide (CuO) is p-type semiconductor with indirect energy band gap of 1.4-1.8 eV. It is efficiently used for water splitting due to the photocatalytic activity as its conduction and valence bands narrowly straddle the water redox potentials. However, it shows relatively lower efficiency to

convert sunlight into hydrogen [31-33]. It may be expected that CuO is an ideal material as a solar cell due to its energy band gap (1.4-1.8eV), which includes the ideal value of solar radiation conversion (1.5eV). However, due to the ohmic losses and overpotentials in photoelectrical and photoelectrochemical systems, this material does not keep this position [34,35].

2. Experimental Part

Titanium dioxide from NanoShell Company with purity of 99.99% and cadmium oxide with purity of 99.99% were mixed at different concentrations of cadmium oxide (0.0, 0.05, 0.1, 0.15 and 0.2 wt.%). The powder of precursor was mixed together using agate mortar and the mixture was then pressed into pellets of 1.5 cm in diameter and 0.2 cm in thickness, using SPECAC hydraulic press under pressure of 5 tons. The pellets were sintered in air at temperature of 773 K for 3 hours.

The $TiO_{2(1-x)}CuO_x$ films were deposited on 10×10 mm glass substrates at room temperature and different concentrations of CuO. The glass substrates were cleaned with diluted water using ultrasonic process for 15 minutes to deposit the films at room temperature then anneal them at 423 and 523 K by a furnace under vacuum ($8x10^{-2}$ mbar). Finally, thin films of TiO_2:CuO were deposited by PLD technique using a 1064nm Q-switched Nd:YAG laser with pulse energy of 800 mJ, repetition frequency of 6 Hz for 500 laser pulses incident on the target surface making an angle of 45°, as shown in Fig. (1).

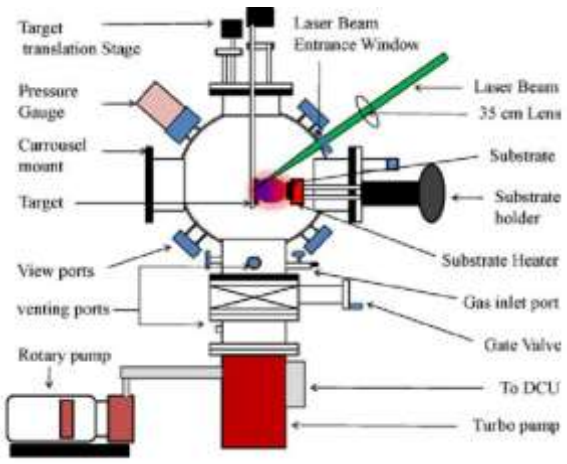

Fig. (1) Experimental setup of PLD system used in this work

The distance between the target and laser was set to 10 cm, and between the target and substrate was 1.5 cm, under vacuum of 8×10^{-2} mbar. The thickness of $TiO_{2(1-x)}CuO_x$ thin films was measured using an optical interferometer method employing 632.8nm He-Ne laser with incident angle of 45°. This method depends on the interference of laser beam reflected from thin film surface and then substrate.

The photoluminescence spectra were recorded using Edinburgh Instrument model FLS920 in the spectral tange of 200-1000nm.

3. Results and Discussion

The photoluminescence (PL) of the 200nm-thick $TiO_{2(1-x)}CuO_x$ films deposited at room temperature and different concentrations of CuO (x=0.0, 0.05, 0.1, 0.15, 0.2 wt.%), and annealed at different temperatures (423 and 523 K) for one hour under vacuum pressure of $8x10^{-2}$ mbr were measured using 150 W xenon arc lamp, in the range of 200-1000 nm at photo-excitation wavelength of 350 nm.

Figure (2) shows the photoluminescence spectra of the $TiO_{2(1-x)}CuO_x$ films prepared at room temperature and different concentrations, and annealed at different temperatures.

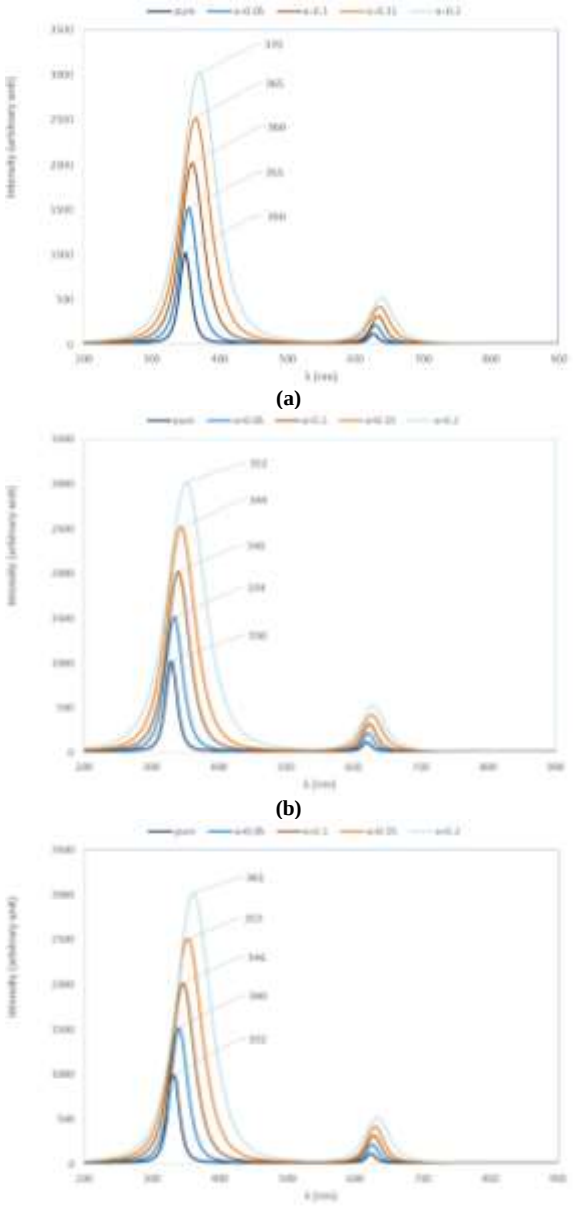

(a)

(b)

(c)

Fig. (2) Photoluminescence spectra for CuO-doped TiO_2 thin films (a) at room temperature, (b) at annealing temperature of 423K, and (c) at annealing temperature of 523K

Typical luminescence behavior with two emission peaks was observed and the UV photoluminescence characteristics of $TiO_{2(1-x)}CuO_x$ films showed strong relation with the temperature. The first peak in photoluminescence spectra between 320-400 nm corresponds to the direct recombination between electrons in the conduction band and holes in the valence band.

In all samples (undoped and doped), a broad peak was also observed at a lower energy or visible region (the second peak). The intensity of the two peaks apparently increases with the increase of concentration due to the large exciton bending energy of $TiO_{2(1-x)}CuO_x$ compound. Higher energy (shorter wavelength) excitation photons cause more phonons to emit before the occurrence of luminescence. If the excitation energy is lower than the energy difference between the ground and first excited states, then no optical absorption will occur, and hence no photoluminescence will result.

Table (1) Peak wavelengths of photoluminescence spectra and energy band gap of the prepared samples

T_s (K)	Content (x)	Wavelength (nm)	E_g (eV)
		First peak	
R.T.	0	350	3.543
	0.05	355	3.493
	0.1	360	3.444
	0.15	365	3.397
	0.2	370	3.351
423	0	332	3.735
	0.05	340	3.647
	0.1	346	3.584
	0.15	353	3.513
	0.2	361	3.435
523	0	330	3.758
	0.05	334	3.713
	0.1	340	3.647
	0.15	344	3.605
	0.2	352	3.523

T_s (K)	Content (x)	Wavelength (nm)	E_g (eV)
		Second peak	
R.T.	0	627	1.978
	0.05	630	1.968
	0.1	634	1.956
	0.15	636	1.950
	0.2	639	1.941
423	0	624	1.987
	0.05	626	1.981
	0.1	628	1.975
	0.15	630	1.968
	0.2	633	1.959
523	0	620	2.000
	0.05	622	1.994
	0.1	624	1.987
	0.15	627	1.978
	0.2	629	1.971

The photoluminescence emission may have close relation with the luminescence of the recombination of photo-induced electrons and holes. The free and self-trapped electron-hole pairs or excitons are possibly resulted from the non-integrality of nano-sized TiO_2 crystallites such as the lattice distortion and surface oxygen deficiencies. However, in thin films, the broad visible emission band at 620-680 nm could be attributed to the self-trapped excitons of the charge transfer process. Table (1) shows the peak wavelengths of photoluminescence spectra and energy and gaps of all samples prepared in this work.

4. Conclusion

In concluding remarks, $TiO_{2(1-x)}CuO_x$ thin films were deposited by PLD technique on glass substrates at different concentrations of CuO at room temperature and then annealed at different temperatures (423 and 523K). Annealing of these films in vacuum for one hour improves the film quality as the doping level is increased. Two emission peaks were observed from photoluminescence analysis, UV photoluminescence characteristics of for undoped and CuO-doped TiO_2 and the intensity gradually increases by increasing the doping level.

References

[1] F. Zaera, "Nanostructured materials for applications in heterogeneous catalysis", Chem. Soc. Rev., 42(7) (2013) 2746-2762.
[2] O.A. Hamadi, "Profiling of Antimony Diffusivity in Silicon Substrates using Laser-Induced Diffusion Technique", Iraqi J. Appl. Phys. Lett., 3(1) (2010) 23-26.
[3] M. Ge et al., "A review of TiO_2 nanostructured catalysts for sustainable H_2 generation", Int. J. Hydrogen Energy, 42(12) (2017) 8418-8449.
[4] U.G. Akpana and B.H. Hameed, "The advancements in sol–gel method of doped-TiO_2 photocatalysts", Appl. Catal., A, 375(1) (2010) 1-11.
[5] S.R. Kurtz and R.G. Gordon, "Chemical vapor deposition of doped TiO_2 thin films" Thin Solid Films, 147(2) (1987) 167-176.
[6] G. Liu et al., "The preparation of Zn^{2+}-doped TiO_2 nanoparticles by sol–gel and solid phase reaction methods respectively and their photocatalytic activities", Chemosphere, 59(9) (2005) 1367-1371.
[7] N. Liu et al., "A review on TiO_2-based nanotubes synthesized via hydrothermal method: Formation mechanism, structure modification, and photocatalytic applications", Catalysis Today, 225 (2014) 34-51.
[8] Z. Dargahi, H. Asgharzadeh and H. Maleki-Ghaleh, "Synthesis of Mo-doped TiO_2/reduced graphene oxide nanocomposite for photoelectrocatalytic applications", Ceram. Int., 44(11) (2018) 13015-13023.
[9] N.S.P. Bhutanese, J. Gopalakrishnan, J. Mater. Chem. 7, 2297 (1997).
[10] A.L. Linsebigler, G. Lu, J.T. Yates Jr., Chem. Rev. 95, 735 (1995).
[11] G.S. Oehrlein, J. Appl. Phys. 59, 1587 (1986).
[12] L. Messick, J. Appl. Phys., 47, 4949 (1976).

[13] R. Mechiakh, R. Bensaha, J. Cond. Mater., 7, 54 (2006).
[14] Y. Leprince-Wang and K. Yu-Zhang, Surf. Coat. Technol., 140, 155–160 (2001).
[15] A. Gjevori," Phase Formation of Photoactive TiO_2 Thin Films by Metal Plasma Immersion Ion Implantation and Deposition", M.Sc. thesis, University of Tirana, Faculty of Natural Sciences (2010).
[16] B. Morris Henry, US Patent 4,200,474 (1978).
[17] M.R. Kozlowski, P.S. Tyler, W.H. Smyrl, R.T. Atanasoki, J. Electrochem. Soc., 136 (1989) 442.
[18] M. Lottiaux, C. Boulesteix, G. Nihoul, et al., Thin Solid Films 170, 107 (1989).
[19] K.S. Yeung, Y.W. Lam, Thin Solid Films 109, 405 (1983).
[20] L.M. Williams, D.W. Hess, J. Vac. Sci. Technol. A 1, 1810 (1983).
[21] O.A. Hammadi, Iraqi J. Appl. Phys. (IJAP), 4(3) 34-37 (2008).
[22] K.A. Vorotilov, E.V. Orlova, V.I. Petrovsky, Thin Solid Films 207, 180 (1992).
[23] M. Gartner, C. Parlog, P. Osiceanu, Thin Solid Films, 234, 561 (1993).
[24] M.H. Suhail, G. Mohan Rao, S. Mohan, J. Appl. Phys. 71, 1421 (1992).
[25] L.-J. Meng, M. Andritschky, M.P. dos Santos, Thin Solid Films 223, 242 (1993).
[26] G. Lazar, I. Vascan, Rom. J. Phys. 43, 571 (1998).
[27] H. Tang, K. Prasad, R. Sanjines, P.E. Schmid, F. Levy, J. Appl. Phys. 75 ,4, 2042 (1994).
[28] H. M. Smith, A. F. Turner, Appl. Opt. 4, 147 (1965).
[29] K.S. Khashan and O.A. Hamadi, "Features of spot-matrix surface hardening of low-carbon steel using pulsed laser", Eng. Technol. J., 25(2) (2007).
[30] Dijkkamp, T. Venkatesan, X. D. Wu, S.A. Shareen, N. Jisnari, Y., Appl. Phys., 51, 619 (1987).
[31] O.A. Hamadi, Proc. IMechE, Part L, J. Mater.: Design and Applications (JMDA), 222, 65-71 (2008).
[32] R. Ferro and J. A. Rodriguez, Sol. Energy Mater. Sol. Cells 64, 363 (2000).
[33] T. K. Ssubramanyam, S. Uthanna and B. Srinvasulu Naidu, Mater. Lett. 35, 214 (1998).
[34] P. R. Patil, P. S. Patil and C. D. Lokhande, Ind. J. Phys. 266, 14 (1995).
[35] M.A. Hameed, S.H. Faisal and R.H. Turki, Iraqi J. Appl. Phys., 16(4) (2020) 25-30.

IRAQI JOURNAL OF APPLIED PHYSICS
Vol. 17, No. 4, October-December 2021, pp. 19-22

Rasul M. Ismaylov
Naske Y. Rahimov

Department of Physic,
Faculty of Science,
University of Koshmanov,
Dushanbe, TAJIKISTAN

Determination of Electronic Properties of Gallium Nitride Structure Using Density Functional Theory

In this work, the density functional theory was used to determine the electronic and related properties of gallium nitride. The results of this work include electronic energy band gap at room temperature as the energy band gap increases with size. It was found that the bond length is within the distribution range. Tetrahedral and dihedral angles approach values of bulk gallium nitride up to higher structural configurations. The density of energy states was varied from approximately single levels to band structure.

Keywords: Gallium nitride; Crystal structure; Density functional theory; Electronic properties

1. Introduction

The study of various Heusler alloys decades ago resulted in the serendipitous discovery of half-metallic (HM) magnetism [1,2]. Next, HM Ferro-magnets aroused interest for its applicability as a spintronic material because they possess one electron spin channel at the Fermi energy level. This results in 100% polarization of the spin carriers [3-5]. Based on the properties of HM compounds, several studies have been carried out to understand their magnetic mechanistic and implications on the physics properties of materials [6-11].

Half-metallic ferromagnets (HMF) such as the alkaline earth pnictides [12], carbides [13,14] and nitrides [15-17] contains no transition metals and rare earth ions exhibits different mechanism for their magnetism compared with those that contain those ions [18]. The magnetism in these compounds is related to the *s* and *p* atomic orbitals and not *d* or *f* atomic orbitals. The ferromagnetic coupling mechanism varies from the *p-d* and double exchange which are vital in 3*d* magnetic systems [19,20].

Gallium nitride (GaN) is a promising material in the development of short-wavelength light emitting devices [21]. The density functional theory is used with the local density approximation as implemented in the O(N) pseudopotential LCAO OpenMX package to calculate the band structure and electronic properties of wurtzite GaN nanowires (GaN NWs) and hydrogen-passivated GaN nanowires [22-24].

Most nitride structures consist of a diamond-like carbon cage, where all atoms are sp^3 hybridised, and dangling bonds at the edges of the systems are terminated with hydrogen atoms. They have the shape of cages that are added together to form nanocrystals and bulk. Present trend in molecular electronics is to manufacture single molecules that should be the ultimate smallest possible electronic component. These molecules should have exceptional stability that can endure applied electrical or magnetic fields that are applied due to electronic signals [25]. In general, they are strong, cage-like structures that differ from other molecules in the bonding of their surface atoms by one or two hydrogen atoms. This structure results in the bonding of these surface atoms to the core of the molecular nanocrystal by at least two bonds, which enhances their stability [26]. Boron phosphide is an indirect gap semiconductor. Under ambient conditions, it crystallizes in the zinc-blende (zb) structure [27]. Gallium nitride (GaN) has a very high thermal conductivity, a significant hardness, and an indirect band-gap [28]. Because of these properties, gallium nitride is useful in high temperature electronics applications and electro-optical devices in the short-wavelength range of the visible spectrum [29].

The density functional theory (DFT) at generalized gradient approximation level of Perdew, Burke, and Ernzerhof (PBE) is used. 6-31G(d) basis set that contains polarization functions are incorporated in present calculations. All calculations are performed using Gaussian 09 program. Density functional theory (DFT) for its successful handling of many properties especially the electronic structure however knowing that Kohn-sham DFT is insufficient method for its deficiencies concerning the gap issue and the long rang interactions approximations. Half-magnetic materials are cage shaped structures discovered in petroleum. These cages are stable and strong since all the constituting atoms (except hydrogen atoms) are connected to bulk of molecule by two or more bonds. Nomenclature of half-magnetic materials follows the number of cages in each half-magnetic material. As an example, diamantane contains two cages while octamantane contains eight cages [30] as shown in Fig. (1).

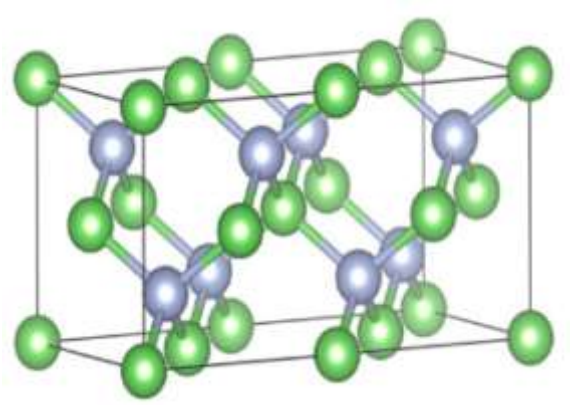

(a) $B_7P_7H_{20}$

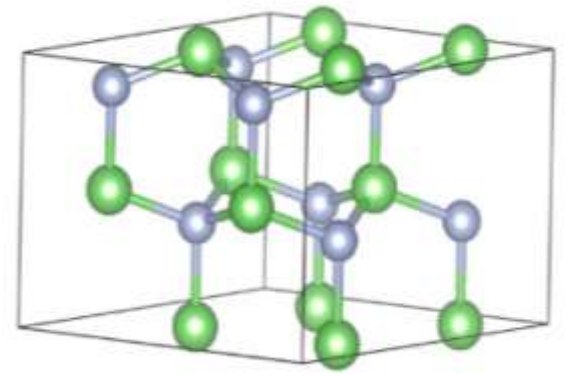

(b) $B_{11}P_{11}H_{28}$

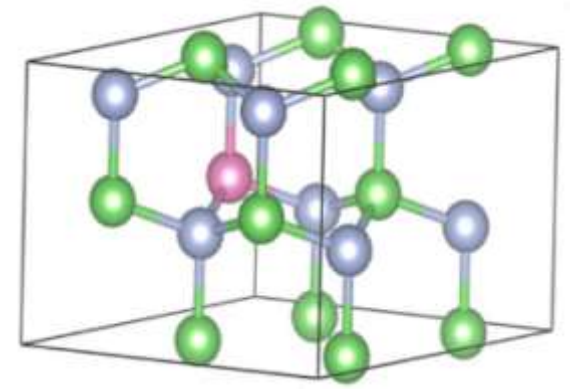

(c) $B_{13}P_{13}H_{30}$

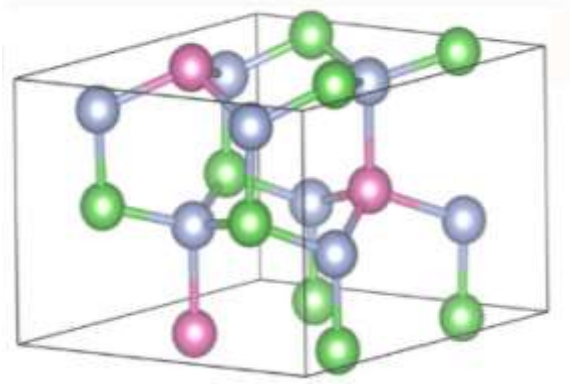

(d) $B_{20}P_{20}H_{42}$

Fig. (1) Instrumentation of geometry of (a) GaN-diamantane, (b) GaN-tetramantane, (c) GaN-hexamantane, (d) GaN-octamantane molecules

2. Results and Discussion

The differences between the energy gap of the smallest half-magnetic materials were considered herein. GaN-diamantane and GaN-octamantane. Energy levels are nearly discrete in GaN-diamantane. As the number of energy levels increases, discrete behavior in GaN-diamantane turns to nearly continuous band in GaN-octamantane. Energy gap reduces from 3.4 eV in GaN-diamantane to 1.7 eV in GaN-octamantane. This reduction is in compliance with confinement effects that require size reduction of energy gap as manifested in Fig. (3) [31]. As in Fig. (2), the smallest gap recorded in our calculations is 1.7 eV for GaN-octamantane. Highest occupied molecular orbital (HOMO) and lowest unoccupied molecular orbital (LUMO) have all negative values (Fig. 3). HOMO and LUMO levels are sometimes used as approximations of ionization energy and electron affinity respectively [32,33], these values show that extraction of an electron or addition of an external electron requires an external energy.

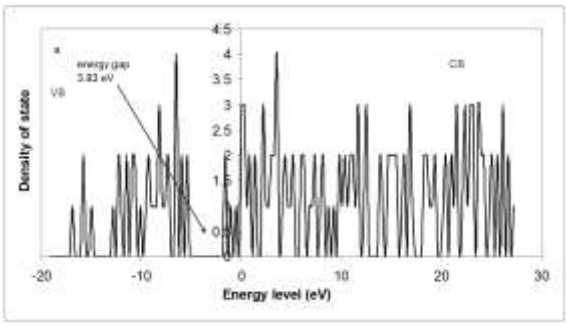

(a)

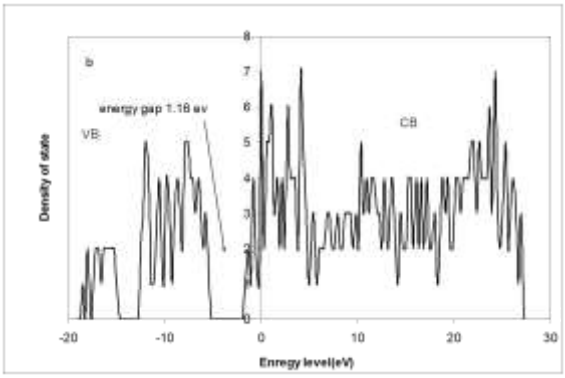

(b)

Fig. (2) Density of state of (a) GaN-dimantane and (b) GaN-octamantane

Bond lengths of GaN-diamantane and GaN-octamantane. Shortest bonds are P-H and B-H respectively. Small number of bonds in GaN-diamantane does not allow the true statistical features of these bonds. In GaN-octamantane B-H bond is a sharp high peak while P-H is a wide base and low height peak. The reason for this is that P is a nonmetal that strongly localize electrons in its bonds. On the contrary B is a semiconductor that has relatively more delocalized electrons in its bonds. The B-P bond has

several peaks depending on number of hydrogen atoms attached to B and P atoms. In B-P-diamantane the smallest value of this bond is when both B and P are connected to single hydrogen atom. These have the value 1.92Å that corresponds to the highest peak for diamantane. The longest bond is at 1.98Å near the far ends of diamantane molecule in which one of the core atoms (Ga or N) is connected to two hydrogen atoms. The location of the bond in the molecule affects its value that explains the several peaks for GaN-diamantane, GaN-octamantane on the other hand have a different situation that spectrum of bonds in case of GaN-octamantane has the range1.93-2Å, with the highest peak at 1.97Å. Experimental bond length of bulk GaN (1.96Å) is within GaN-diamantane and GaN-octamantane bond distribution (Fig. 4).

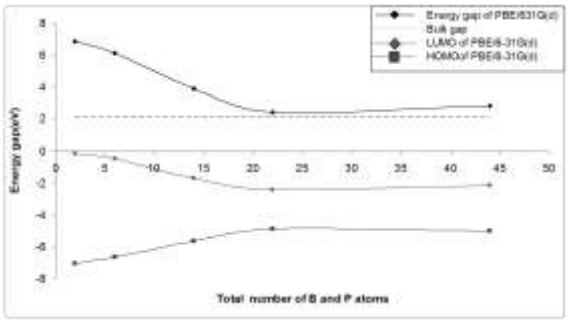

Fig. (3) Energy gap, HOMO and LUMO levels as a function of total number of gallium and nitrogen atoms in gallium nitride structure using PBE/6-31G (d)

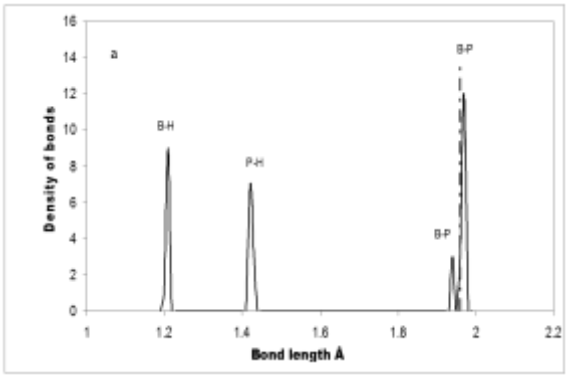

(a)

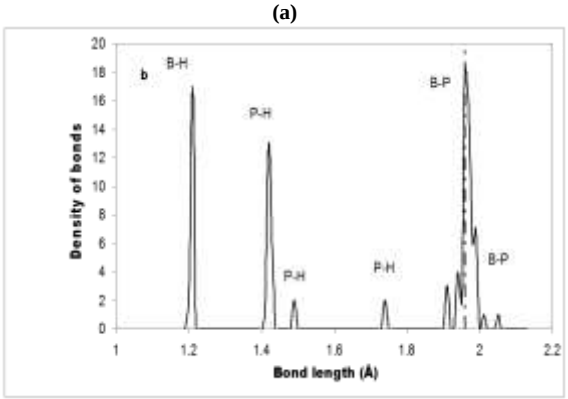

(b)

Fig. (4) Density of bonds in GaN-diamantane and density of bonds GaN-octamantane. Dashed line represents the experimental GaN bond length at 1.96Å

Figure (5) shows a comparison between density of tetrahedral angles in GaN-diamantane and density of tetrahedral angles in GaN-octamantane. In a piece of bulk far from surface all tetrahedral angles should have the value 108.57° [11]. As we can see from Fig. (5), the highest peak of GaN-diamantane is at 110.9°, while that of GaN-octamantane is at 105.47°, Tetrahedral angles of diamantane are much closer to the ideal value 108.57°than that of octamantane. This is due to the effect of surface reconstruction that has an effect on all atoms in GaN-diamantane and GaN-octamantane (all the atoms are bonded to surface hydrogen atoms).

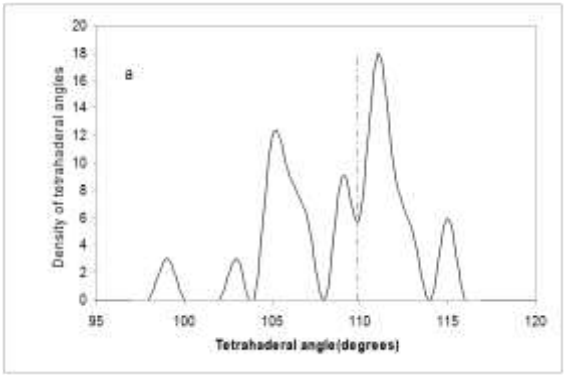

(a)

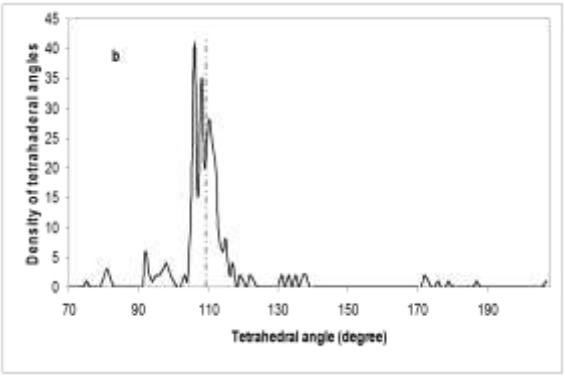

(b)

Fig. (5) Density of tetrahedral angles in (a) GaN-diamantane (b) GaN-octamantane. The dashed line represents the ideal value of zinc-blende structure at 108.57°

Similarly, all dihedral angles should have a value of the following: -180°, -60°, 60° and 180° in bulk zinc-blende structure [34,35]. This may be correct for the angle values of ±180° in GaN-diamantane, GaN-octamantane. It is not totally correct for the angle values of -60° and 60°. For GaN-octamantane, the situation improves for the angles near -60° and 60° that become closer to their ideal values in Fig. (6).

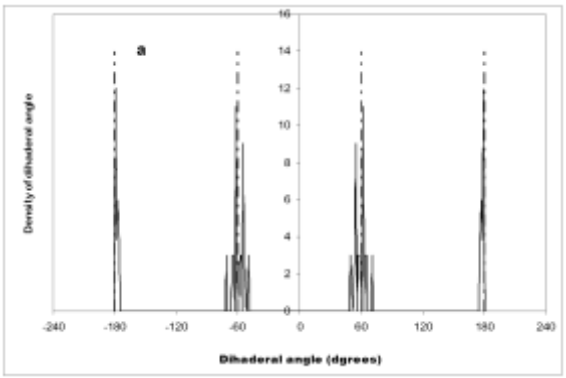

(a)

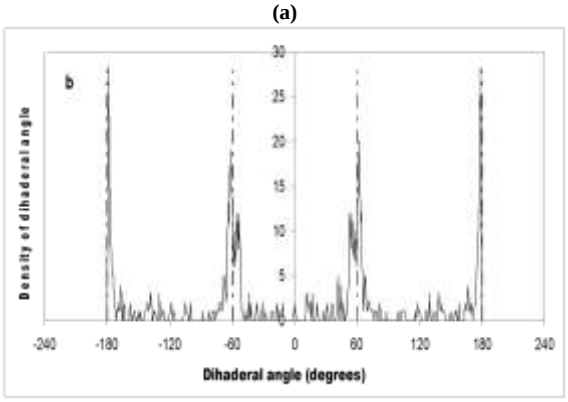

(b)

Fig. (6) Density of dihedral angles in (a) GaN-diamantane (b) GaN-octamantane, PBE/6-31G (d) basis sets is used. Dashed lines show the ideal value of this angle in bulk zinc-blende crystals, i.e., ±60° or ±180°

3. Conclusions

Half-magnetic materials are suggested to be building blocks of GaN nanocrystals and bulk. We can benefit from these structures to monitor how GaN nanocrystals and bulk properties are reached from their corresponding molecular properties. Half-magnetic materials show minimal surface relaxation effects, which can be deduced from their bond lengths, tetrahedral angles and dihedral angles, Energy gap, bond length. B-P bond lengths are affected by surface reconstruction. The shortest B-P bond is between the atoms that are not connected to surface hydrogen atoms. Tetrahedral and dihedral angles converge to their ideal zinc-blende values as we reach higher size structures. Density of energy states show the transition from single energy levels to band structure as we reach higher size structures.

References

[1] R. De Groot, F. Mueller, P. Van Engen, K. Buschow, Phys. Rev. Lett., 50 (1983) 2024.
[2] H. van Leuken, R.A. de Groot, Phys. Rev. Lett., 74 (1995) 1171-1173.
[3] O.A. Hamadi, R.A. Markub and A.A.K. Hadi, J Edu. Al-Mustansiriya Univ., 3 (2001) 35-44.
[4] M. Katsnelson et al., Rev. Mod. Phys., 80 (2008) 315.
[5] J. Coey and M. Venkatesan, J. Appl. Phys., 91 (2002) 8345-8350.
[6] K. Russell et al., Appl. Phys. Lett., 85 (2004) 4502-4504.
[7] R.A. Ismail, O.A. Abdulrazaq, A.A. Hadi and O.A. Hamadi, Int. J. Mod. Phys., 19(31) (2005) 4619-4628.
[8] K. Sato et al., Rev. Mod. Phys., 82 (2010) 1633.
[9] A. Djefal et al., Spin, 7 (2017) 1750009.
[10] O.A. Hamadi, S.M. Hussain, A.A. Hadi and R.O. Mahdi, Eng. Technol. J., 27(4) (2007).
[11] L. Seddik et al., Spin, 7 (2018) 1750010.
[12] K. Kusakabe et al., J. Phys.: Cond. Matter, 16 (2004) S5639.
[13] O.A. Hamadi, Iraqi J. Appl. Phys. Lett., 3(1) (2010) 23-26.
[14] G.Y. Gao, K.L. Yao and N. Li, J. Phys.: Cond. Matter, 23 (2011) 075501.
[15] F.J. Kadhim and A.A. Anber, J. Indust. Eng. Sci., 25(5) (2016) 91-94.
[16] O.A. Hammadi, Adv. Sci. Eng. Med., 11(5) (2019) 346-350.
[17] O.A. Hammadi, Mater. Res. Exp., 8(8) (2021) 085013.
[18] F.J. Kadhim, O.A. Hammadi and A.A. Anber, Iraqi J. Appl. Phys., 17(2) (2021) 9-12.
[19] G.Y. Gao et al., Phys. Rev. B, 75 (2007) 174442.
[20] O. Volnianska, P. Jakubas and P. Bogusławski, J. Alloys Comp., 423 (2006) 191-193.
[21] Y. Bourourou et al., J. Magn. Mag. Mater., 365 (2014) 23-30.
[22] O.A. Hammadi, M.K. Khalaf and F.J. Kadhim, Proc. IMechE, Part N, J. Nanomater. Nanoeng. Nanosys., 230(1) (2016) 32-36.
[23] V.F. Hlynsson, E. Skúlason and A.L. Garden, J. Alloys Comp., 603 (2014) 172-179.
[24] B. Eck et al., J. Mater. Chem., 9 (1999) 1527-1537.
[25] J. E. Dahl, S. G. Liu, and R. M. K. Carlson, Sci. 299, 96 (2003).
[26] G. Davies et al., Nanomater. Nanotechnol., 7 (2017) 21-30.
[27] O. Madelung, Semiconductors: Data Handbook, 3rd ed. (Springer, 2004).
[28] O.A. Golikova, phys. stat. sol. A, 51(1), 11–40 (1979).
[29] S. Cui, W. Feng, H. Hu, Z. Feng, and Y. Wang, Comput. Mater. Sci., 44(4), 1386–1389 (2009).
[30] N. Bites, R. Renolds and J. Coin, Phys. Mater. Commun., 5 (2020) 103-108.
[31] H. Mittler, Physica E, 45 (2013) 431-435.
[32] Sque S J, Jones R, Briddon P. R Phys. Rev. B 73: 085313. (2006)
[33] O.A. Hammadi, M.K. Khalaf and F.J. Kadhim, Proc. IMechE, Part L, J. Mater.: Design & Appl., 231(5) (2017) 479-487.
[34] C. Morley et al., Appl. Phys. Res., 21 (2018) 15-20.
[35] A. Q. Zhou, C. S. O'Hern, and L. Regan, Biophys. J. 102, 2345 (2012).

IRAQI JOURNAL OF APPLIED PHYSICS
Vol. 17, No. 3, July-September 2021, pp. 23-28

Preparation of Zirconia Aerogel Nanostructures by Supercritical Drying Autoclave Method

Mehta Raj Kumar
Vijay Revonda

Department of Materials Engineering,
Faculty of Engineering,
University of Shukla,
Shukla, INDIA

In this work, zirconium dioxide (ZrO_2) aerogel monoliths were successfully prepared using drying autoclave method. The effects of synthesis environment on the morphological, optical and thermal properties of the synthesized monoliths were studied. The implemented autoclave was able to produce aerogel monolith of surface area up to 998.25 g/m^2 and thermal conductivity of 0.0053 mW.m^{-1}.°C, associated with density of 0.047 g/cm^3. It was found that the density, optical transmittance and porosity are strongly affected by the starting pH value as their final microstructures were introduced by scanning electron microscopy (SEM) and Brunauer-Emmett-Teller (BET) method. The lack of catalyst during aerogel preparation has resulted in dense, opaque and less porosity monoliths. As the environment was little basified, the aerogel properties were remarkably varied, while acidifying the reaction setting had gradual influence on the final aerogel properties. However, it is obviously requested for achieving desirable optically and nano-featured products.

Keywords: Aerogel; Supercritical drying; Autoclave method; Nanostructures

1. Introduction

In the last decade, modifications on sol-gel method led to rapid progress in synthesis of porous structures and compounds. These structures and compounds are exceptionally important for different industrial, biological and environmental applications [1-3]. Zirconia aerogel has become very common when compared to other aerogel materials due to its interesting properties, mainly high specific surface area, high porosity, low thermal conductivity, low density and low refractive index [4-6]. Accordingly, many various applications of zirconia aerogel were recently presented [7,8].

In sol-gel method, nanostructured solid networks are formed in a liquid reaction media as a result of hydrolysis followed by polymerization processes creating O-Zr-O bridges between Zr atoms delivered by the precursor molecules, which is zirconyl chloride octahydrate ($ZrOCl_2 \cdot 8H_2O$) [9,10]. The initial product of sol-gel process is the gel, where solvent will completely include the pores of gel. Then the solvent is removed from the gel by a drying step [11]. The main difficulty in drying gel is the occurrence of capillary forces in the pores due to surface tension of the liquid; where under conventional thermal drying the gel undergoes cracking and significant shrinkage (up to a few times its initial volume) [12]. Fundamentally, the fluids that full the pore volume are water as a result of condensation process and alcohol that adopted initially as well as by product of hydrolysis and condensation [13,14]. As a consequence of water have high surface tension compare with alcohols, therefore, we need to sock the gel several times by pure alcohol prior to drying, and to pull water out resulted in alcogel, so that capillary forces will reduced [15]. Zirconia alcogel can be processed in some ways to yield aerogels and the route considered in this work is the production of the zirconia aerogel by supercritical drying method (SCD) [16,17]. By heating and compressing the gel above the critical temperature (T_C) and pressure of its inner solvent, the solvent will be extracted from the gel without generating a two-phase system and hence the capillary forces will be minimized. In the final step, the alcogel inside the autoclave – under supercritical condition – must be cooled down and depressurized from critical point to the ambient condition. In this work, carbon dioxide (CO_2) gas was used as the supercritical fluid [18,19].

2. Experimental Part

The chemicals used in the synthesis were, zirconyl chloride octahydrate ($ZrOCl_2 \cdot 8H_2O$) abbreviated by ZOCW with purity >99.0%, ethyl alcohol (spectroscopic grade, 200 proof >99.5% purity), and deionized water catalyzed by ammonium fluoride (>98.0% purity). Deionized water was catalyzed by hydrochloric acid (0.15 M, >99.0% purity), and by ammonium hydroxide (28-30% concentration).

In order to construct the autoclave, a stainless steel tube of 18 cm diameter and 35 cm in length was used as a reaction chamber. This tube can be efficiently used for high-pressure purposes. High-quality valves were used to control the input and output flows through the chamber as well as to depressurize it. Tab heater and electronic-controlled

thermocouple were also used. Figure (1) shows the autoclave chamber used in this work.

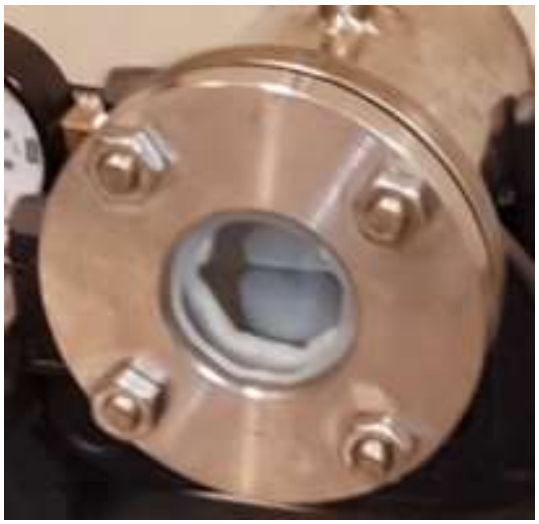

Fig. (1) The autoclave chamber used in this work

The preparation of zirconia gels was consisting of a single-step procedure as follows. The zirconyl chloride octahydrate ($ZrOCl_2 \cdot 8H_2O$), ethanol, water, and hydrochloric acid (or NH_4OH) were mixed at molar ratio of 1:11:10:X, where X was varied to achieve sols of final pH value in the range 1 to 10. These sols were heated to 30 °C for 30 minutes in a magnetic stirrer. After that, a 0.5 ml of C_3H_7NO was added as a drying control chemical additive (DCCA) and kept for 60 minutes in the magnetic stirrer. The resulting sol was poured through a plastic tube of 24.5 mm in diameter and permitted to gelled and aged in the same tube for 28 hours at room temperature (27°C). The gel samples were rinsed with pure ethanol five times during 24 hours. Fresh ethanol was used for each successive step to remove any unreacted monomer that may residue from the gel network.

Zirconia aerogels were prepared using supercritical drying technique (low temperature carbon dioxide solvent exchange). Here, the alcogel is placed inside the autoclave as the sample be moisten at constant drenching with ethanol for 30 minutes. The autoclave was tightly closed and the CO_2 gas was pumped into the autoclave very slowly until reaching pressure of 55 bars with the synchronization process of autoclave cooling to 5 °C until the liquid CO_2 is obtained. This step will enhance the transfer of CO_2 gas from gas into liquid state. The gel sample was separated from the liquid containing it inside the autoclave. These two liquids were kept stable for enough time then the liquid CO_2 was changed more than 4 times for 28 hours to vent all undesired solvents out of the gel. This process makes the alcogel soaking just in CO_2 liquid for further 36 hours. After that, heating process is started by slowly increasing the autoclave temperature using the wire heater to obtain supercritical condition at 73 bar and 32 °C. The temperature and pressure were maintained above the supercritical boundary to achieve the supercritical drying for 2-3 hours with depressurizing process every 30 minutes. Finally, depressurizing process will allowed to continue for few hours to get the zirconia aerogel with uniform shape. All prepared samples were finally kept in an oven at 700°C for one hour. The aerogel samples prepared at different pH values are shown in Fig. (2).

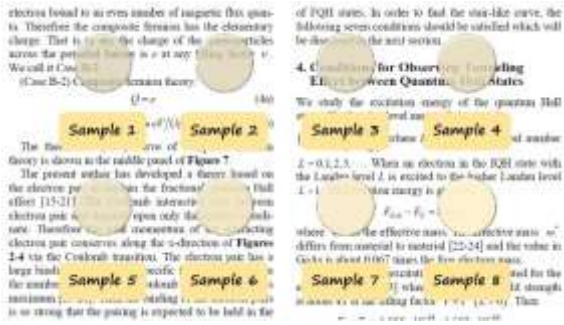

Fig. (2) Zirconia aerogel samples prepared at different pH values

Specific surface area and pore size of prepared aerogel were determined by the Brunauer-Emmett-Teller (BET) method using Micromeritics ASAP 2020 instrument. The microstructure and morphology of aerogel samples were introduced by scanning electron microscopy (SEM). The thermal conductivity of the prepared aerogel was recorded using Lee's disc apparatus. The spectral transmittance of the prepared was recorded by UV-visible spectrophotometer. By weighing cylindrical uniform aerogel samples of precise dimensions, the apparent densities were calculated. The dried aerogels were then annealed by heating up to 700 °C with a heating rate of 60 °C/hr.

3. Results and Discussion

The discussion was focused on three samples those may represent the acidic, neutral and basic environment as their pH values are 1, 7 and 8, respectively. They are denoted by pH1, pH and pH8, respectively. The transmittance spectra of the prepared zirconia aerogel in the entire visible region of these samples are shown in Fig. (3). It is clear that pH7, pH1 and pH8 samples exhibit lowest, moderate and highest values of transmittance, respectively.

The infrared (IR) transmittance spectra of the prepared aerogel samples are shown in Fig. (4). Several absorption bands are seen in these spectra. The formation of zirconia molecules was confirmed by two characteristic vibrational bands, a strong band centered at 460 cm^{-1}, and another strong and broad band at 1104 cm^{-1}. These bands are corresponding to the bending and asymmetric stretching vibrations of (Zr—O—Zr) groups, while the symmetric stretching characteristic zirconia band (O—Zr—O) is weak and seen at 812 cm^{-1} [20,21]. A medium and broad band at 3500 cm^{-1} and a small sharp band at 1650 cm^{-1} are

ascribed to the vibration modes of O–H bond. These two bands confirm the existence of some residual (or adsorbed) free OH groups in the prepared aerogel samples [22,23].

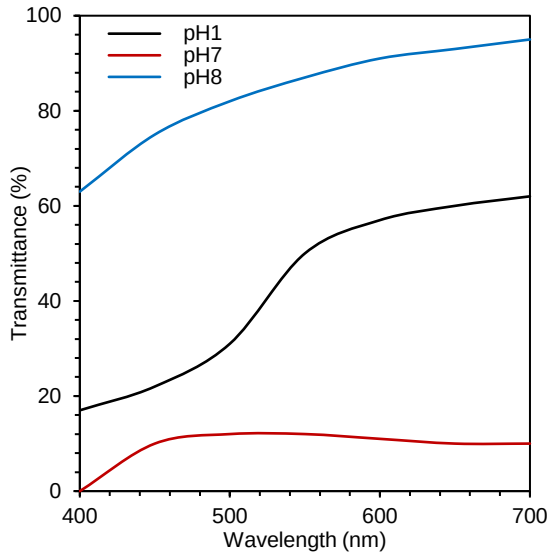

Fig. (3) Transmittance spectra for aerogel samples pH1, pH7 and pH8

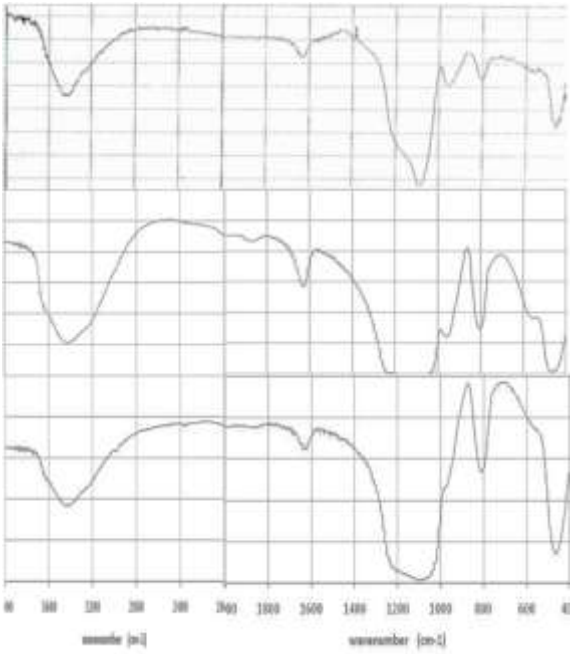

Fig. (4) FTIR transmission spectra for aerogels, pH1 sample (upper), pH7 sample (middle) and pH8 sample (lower)

The FTIR spectra for aerogel sample pH1 at three different annealing temperatures (500, 700 and 900°C) are presented in Fig. (5) while the linear isotherm plots for the aerogel samples prepared at several final pH values are shown in Fig. (6).

Table (1) shows the variation of thermal conductivity, density, transmittance at 550nm, surface area, pore volume, pore size and porosity with the final preparation pH value. Maximum pore size, pore volume and porosity were recorded for pH8 sample, while under neutral environmental, pH7, the product exhibit lowest pore size and volume as well as surface area.

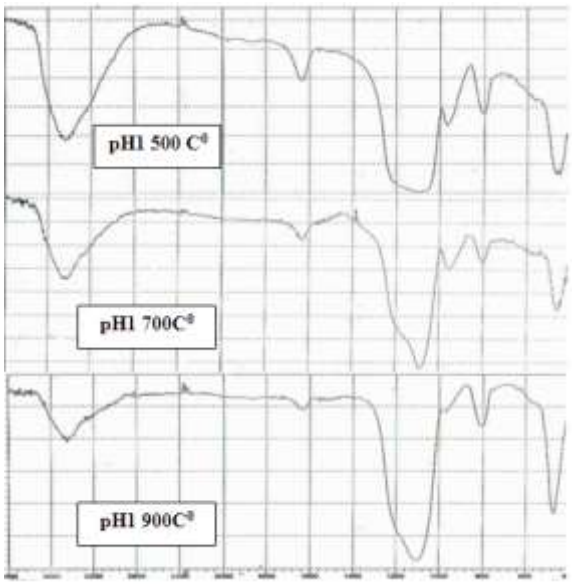

Fig. (5) FTIR spectra for aerogel sample pH1 at three different annealing temperatures (500 °C, 700 °C and 900 °C)

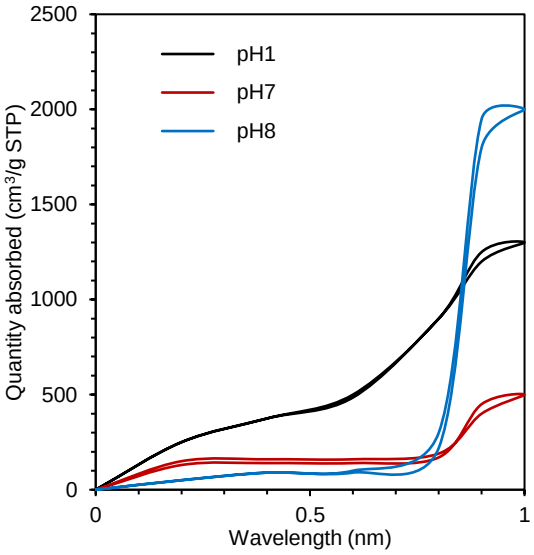

Fig. (6) Linear isotherm plot for three samples prepared at different pH values

Table (1) Summary of properties and structural data of three samples prepared at different pH values

Sample	Surface area (m^2/g)	Pore volume (cm^3/g)	Pore size (Å)	Porosity (%)
PH 1	998.25	1.93	77.71	86.33
PH 7	102.19	0.11	44.91	43.76
PH 8	450.26	2.45	218.28	90.61

Sample	Thermal Conductivity ($mW.m^{-1}.°C$)	Density (g/cm^3)	T (%) @550nm
PH 1	0.0063	0.051	50
PH 7	0.016	0.129	6.8
PH 8	0.0053	0.047	88

Figure (6) shows the SEM images for aerogel sample prepared in acid, base and natural environmental. It is obviously noted that the samples have different network structures related to their pH value. The morphology of these three samples is classified into distinct categories. The pH1 sample is monostructural characterized by a repetition of elongated open cellular foam microstructural features. The pH7 sample has very similar microstructure appears to be fractal in nature with a hierarchical repetition (similar shapes at different length scales). The microstructure of pH8 sample shows an isotropic ultrafine structure.

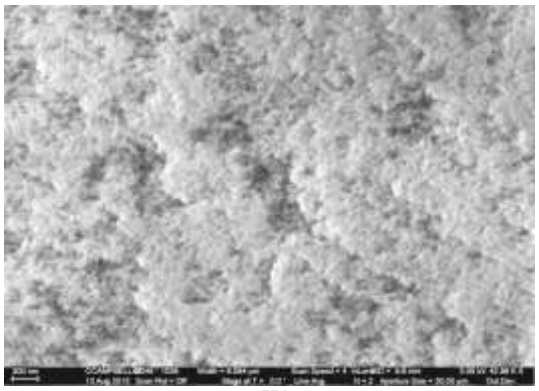

pH1

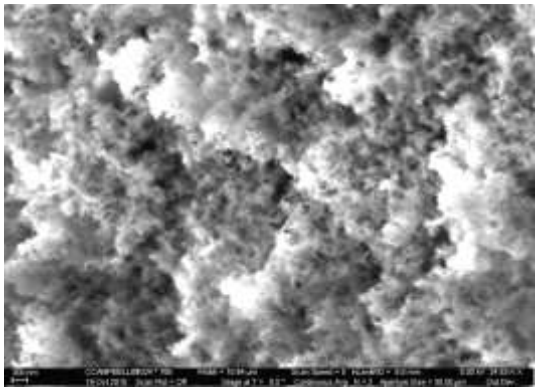

pH7

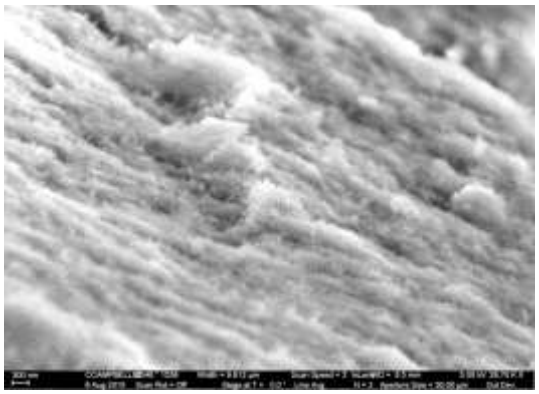

pH8

Fig. (6) SEM images for aerogel samples prepared at different values of pH

Excluding final pH values, the aerogels samples were prepared at the same conditions of reaction temperature, molar ratio (ZOCW: water) and aging time. Accordingly, the pH value was the exclusive varying factor affecting the aerogel microstructure, subsequently followed by other aerogel properties. Commonly, aerogels, as nanoporous materials, have highly transparency and low thermal conductivity [24]. However, acid and base catalysts have significant influence in this matter, where pH8 sample shows higher transmittance while lowest transmittance was shown at natural environment (pH7). Because the lowest reaction rate for hydrolysis occurs at pH=7 [25], many of zirconia networks still unreacted under this condition. Consequently, the electrophilic tendency of condensation terminates and the alcohol condensation mechanism becomes favorable [26,27]. This condition will give rise to more branchy networks, after a while leading to small pore volume and narrow pore size then to lowest transparency of pH7 (Fig. 3 and Table 1).

The EDS spectra shown in Fig. (7) are corresponding to the aerogel samples pH1 and pH7 before densification. They reflect the existence of residual alcohol carbon in pH7 sample, which is lower than that in pH1 sample.

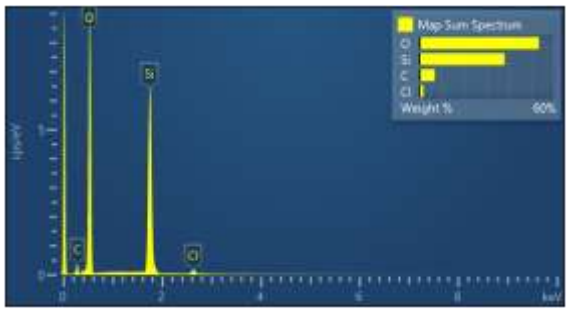

pH1

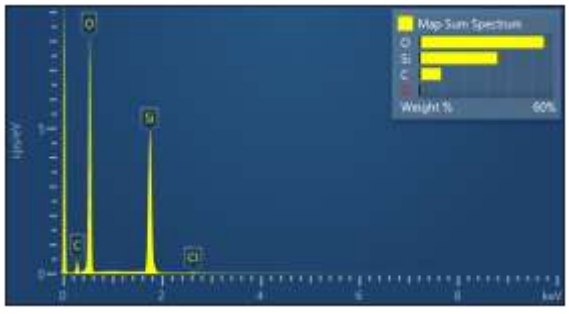

pH7

Fig. (7) EDS spectra for aerogel samples prepared at different values of pH (pH1 and pH7)

The solubility of zirconia is reasonably low in the acidic environment (pH1), therefore, the formation and aggregation of primary particles of zirconia are coordinated as extremely building blocks of small primary particles correlated to high surface area of about 1000 m^2/gm (see table 1). This reaction demands high electron density, therefore, the condensation process will result in more straight

chains. For pH8, condensed species are semi-ionized and therefore, mutually repulsive. Thus, the growth occurs primarily as a result of the addition of monomers to the more highly condensed particles rather than by particle aggregation [28,29]. This semi-ionized feature commonly gives rise to cracking tendency in the preparation of monolithic yielding size limitation. However, this can be overwhelmed using proper amount of DCCA. The transmittance was increased markedly in pH8 sample correlated with ultrafine structure at the nanoscale presented in the morphological SEM image.

Obviously, the FTIR spectroscopy is utilized for qualitative tests. In this work, the samples were prepared under appropriate standards, therefore, the relative amounts of bonds in the different samples can be compared to each other [30,31]. Zirconia aerogels often contain considerable amounts of adsorbed water appeared as a strong, broad band near 3500 cm^{-1} and small sharp at 1650 cm^{-1}. These two bands are ascribed to bending and stretching vibrations of O—H bond in H_2O molecules [32]. These bands are weakened by annealing at 900 °C as the intensities of these band were reduced but not vanished (Fig. 4 and 5). In fact, due to the hydrophilic tendency of zirconia aerogel prepared by supercritical method, the moisture may keep the O-H bond existing even if high temperature is used. Referring to figures (4) and (5), under basic environment, the fast condensation reactions have great chance to complete rather than slow reactions under neutral and acidic environments. Therefore, in case of preparation of optical elements from aerogels, considering anti-liquefaction as well as transparency requirements, it is strongly recommended to consider the preparation conditions of pH8 sample.

The weak band peak fixed at 965 cm^{-1} may be ascribed to stretching vibration of zirconel (Zr—OH) groups [23]. The intensity of this peak was decreasing monotonically with increasing annealing temperature. This may be due to the completion of the condensation reaction with temperature yielding more and more conversion of zirconel bonds to zircoxane bonds (Zr—O—Zr) [33].

The liner isotherm plots presented in Fig. (6) may confirm the above indications. The plots can be examined with the aid of the IUPAC classification hysteresis loops [34]. The hysteresis loops related to pH1 sample can be classified as H3 type which is correlated to non-rigid aggregates of plate-like particles (slit-shaped pores). In case of pH7 sample, the plot may be classified as H4 type which is linked to narrow slit pores including pores in the micropore region. Finally, the plot belonging to pH8 sample can be classified as H1 type, mentioned to well-defined cylindrical pore channels [35].

The lowest thermal conductivity was recorded for pH8 sample, the correlation between the porosity and thermal conductivity of zirconia aerogel as well as lowest density is clearly noticeable. In most cases, the zirconia aerogel possesses very small (1-10%) three dimensional network fraction of solid zirconia. Therefore, the thermal transparent through the solid portion occurs through tortuous path [36].

5. Conclusions

A simple autoclave can used to prepare zirconia aerogel samples of proper physical properties. The structures and optical properties of such aerogels can be controlled by means of suitable selection of initial pH preparation value. Considering basic environment, highly transparent, lower density and crackly monoliths are prepared. On the other hand, using acidic catalyst, smaller particle size, higher surface area and more reactive aerogels are produced. Therefore, low-density thermal insulators, optical windows, and small-pore hydrogen storage tanks can utilize such aerogels by adjusting the starting catalyst.

References

[1] A. Amlouk et al., Mater. Sci. Eng. B, 146(1-3) (2008) 74-79.
[2] C.M. Mo, Y.H. Li and Y.S. Liu, J. Appl. Phys., 83(8) (1998) 4389.
[3] D. Nakashima and R. Ikeda, Phys. Rev. B, 103(6) (2021) 064502.
[4] E. Borsella et al., Mater. Sci. Eng. B, 79(1) (2001) 55-62.
[5] E.E. Carpenter, J. Appl. Phys., 99(8) (2006) 08N711.
[6] F. De Nicola et al., Phys. Rev. Appl., 14(2) (2020) 024022.
[7] G. Zu et al., Micropor. Mesopor. Mater., 238 (2017) 90-96.
[8] H.H. Hamdeh and J.C. Ho, J. Appl. Phys., 81(4) (1997) 1851.
[9] J. Quintanilla, J. Appl. Phys., 93(8) (2003) 4584.
[10] J. Torres-Rodríguez et al., J. Supercr. Fluids, 149 (2019) 54-63.
[11] K. Matsuzawa et al., Mater. Sci. Eng. B, 267 (2021) 115112.
[12] K. Saravanan, B. Tyagi and H.C.Bajaj, Appl. Catal. B, 192 (2016) 161-170.
[13] K. Shu et al., Phys. Rev. B, 104(5) (2021) L050801.
[14] M. Liu et al., J. Appl. Phys., 116(9) (2014) 093503.
[15] M. Obori et al., Phys. Rev. Appl., 11(2) (2019) 024044.
[16] M. Qian, C. Xu and Y. Gao, Mater. Sci. Eng. B, 238-239 (2018) 146-154.
[17] M.A. Worsley, J.H. Satcher Jr. and T.F. Baumann, J. Appl. Phys., 105(8) (2009) 084316.
[18] M.D. Guild et al., Phys. Rev. Appl., 5(3) (2016) 034012.
[19] M.D. Knudson and R.W. Lemke, J. Appl. Phys., 114(5) (2013) 053510.
[20] M.D. Knudson, J.R. Asay and C. Deeney, J. Appl. Phys., 97(7) (2005) 073514.
[21] M.-H. Jo et al., J. Appl. Phys., 82(3) (1997) 1299.

[22] P. Katanyoota et al., Mater. Sci. Eng. B, 167(1) (2010) 36-42.
[23] P. Peshev et al, Mater. Sci. Eng. B, 97(1) (2003) 106-110.
[24] P.E. Hopkins et al., J. Appl. Phys., 111(11) (2012) 113532.
[25] P.E. Stallworth et al., J. Appl. Phys., 92(7) (2002) 3839.
[26] R. Esquivel-Sirvent, J. Appl. Phys., 102(3) (2007) 034307.
[27] Rege, S. Aney and B. Milow, Phys. Rev. B, 103(4) (2021) 043001.
[28] S.A. Bahrani, Y. Jannot and A. Degiovanni, J. Appl. Phys., 116(14) (2014) 143509.
[29] S.O. Kocheyev et al., J. Appl. Phys., 101(12) (2007) 124315.
[30] T. Coquil et al., J. Appl. Phys., 106(3) (2009) 034910.
[31] T. Hisamitsu and R. Ikeda, Phys. Rev. B, 103(17) (2021) 174503.
[32] V.V. Dmitriev, A.A. Soldatov and A.N. Yudin, Phys. Rev. B, 120(7) (2018) 075301.
[33] X. Lu, O. Nilsson and J. Fricke, J. Appl. Phys., 73(2) (1992) 581.
[34] Y. Kong, X. Shen and S. Cui, Micropor. Mesopor. Mater., 236 (2016) 269-276.
[35] Y. Lee et al., Appl. Catal. A, 506 (2015) 288-293.
[36] Y. Zhang et al., Mater. Sci. Eng. B, 188 (2014) 13-19.

IRAQI JOURNAL OF APPLIED PHYSICS
Vol. 17, No. 4, October-December 2021, pp. 29-32

Preparation and Structural Characterization of Cu_2ZnSnS_4 Thin Films by Quenching-Assisted Coating Method

Otkedma Axoke

Department of Physics, Faculty of Science, University of Zululand, KwaDlangezwa 3886, SOUTH AFRICA

In this work, the role of substrate temperature on the structure and microstructure of Cu_2ZnSnS_4 thin films was investigated. The results showed that the structure was amorphous for as-deposited films while it was polycrystalline for films prepared at elevated temperature. The grain size decreased while roughness increased with increasing substrate temperature. The obtained results gave indication that there is a relation between the structure and preparation temperature as well as heat treatment.

Keywords: Cu_2ZnSnS_4 semiconductor; Thin films; Heterojunction; Quaternary compounds

1. Introduction

A promising candidate for low cost absorber layers is the quaternary compound Cu_2ZnSnS_4 (CZTS) which is an analogue of $CuInS_2$ (CIS) obtained by replacing In(III) by Zn(II) and Sn(IV) in a 50:50 ratio. This direct bandgap p-type semiconductor [4], which has received remarkably little attention in the literature, contains only abundant non-toxic elements. The band gap values reported for CZTS (1.45-1.6 eV) [5-7] fall within the optimum range for a single junction terrestrial solar cell. CZTS has been prepared by Katagiri and co-workers, who used inline vacuum sputtering of Cu, SnS and ZnS followed by annealing in a hydrogen sulfide atmosphere [5,8]. Initial attempts to fabricate photovoltaic devices with these CZTS films led to promising results, with AM 1.5 efficiencies of up to 5.7% [5].

The quaternary compounds (CuZnSeTe, CuZnSeS and Cu_2ZnSnS_4) are considered as absorbing materials for solar cell applications. There are few data available about their bulk material properties [1-3] as well as thin films [4-7]. The available data refer that there is a strong dependence between their structure and preparation conditions, which may be due to the amorphous nature as well as the dependencies of their properties on the ambient conditions. The electrical properties and optical properties for Cu_2ZnSnS_4, CuZnSeTe and CuZnSeS thin films were intensively studied [8-13].

CZTS whose crystal structure is shown in Fig. (1) is promising as it replaces rare and expensive In, Ga in commercial $CuIn_XGa_{(1-X)}Se_2$ (CIGS) solar cells with earth-abundant and cheap Zn, Sn, which could reliably support terawatt renewable electricity consumption [14]. Meanwhile it shares similar properties with CIGS. CZTS at this stage mainly imitates the processing of CIGS as a shortcut for development. Co-evaporation is proved a successful technique in achieving the record 21.7% CIGS solar cell efficiency [15]. Besides this, sequential evaporation of the elements or compound often shows strong inhomogeneity and multi-phases [16]. Additionally, a close to stoichiometry pure sulphide CZTS solar cell has achieved 4.1% by one step co-evaporation without further sulfurization [17]. Moreover, chemical composition is one of the major factors to influence efficiency [18]. Therefore, co-evaporation of CZTS and chemical composition inhomogeneity of the evaporated film is continuously investigated.

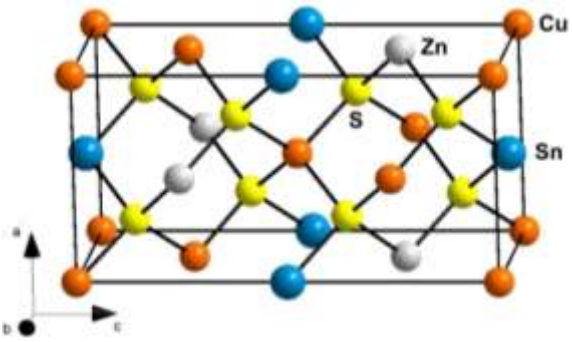

Fig. (1) Crystal structure of Cu_2ZnSnS_4

Chemical composition non-uniformity is not an issue for CIGS solar cell, however may form a major challenge for CZTS solar cells. CIGS has a wide range of tolerance of the anion-to-cation off-stoichiometry [19]. However, CZTS has a narrow chemical composition window for a single phase CZTS absorber [20]. Meanwhile, empirically a sweet chemical range for high efficiency CZTS solar cells has been identified: ratio of Cu/(Zn+Sn)=0.8-0.9 and Zn/Sn=1.2-1.3 [18]. It implies the tolerance for the composition variation: (0.9-0.8)/0.8=12.5% for Cu/(Zn+Sn) and (1.3-1.2)/1.2=8.33% for Zn/Sn. As Cu/Sn ratio appears to be also important [21], it was also included in this study. Even at compositions in this range, the efficiencies reported by different

groups could have a difference above 10% [18]. This paper is to reveal whether composition uniformity is an issue for future CZTS production [22,23].

This work is devoted to perform quaternary alloy of Cu_2ZnSnS_4 and then to prepare thin films at various substrate temperatures and point out the dependencies of dielectric and structural properties on deposition condition using relation between the preparation temperature and these properties.

2. Experimental Part

The alloys of Cu_2ZnSnS_4 were prepared by quenching technique. The exact amounts of high purity (99.999%) copper (Cu), zinc (Zn), selenium (Se) and sulphur (S) were used to form mixtures. These mixtures were sealed in quartz ampoules evacuated down to 10^{-3} torr. These ampoules containing the mixtures were heated up inside a furnace to 1000 °C and frequently rocked at the highest temperature for 10 hours. The quenching step was carried out in water immediately after taking out the ampoules from the furnace. The Cu_2ZnSnS_4 thin films were deposited on substrates of different temperatures (30, 100, and 150°C) using an Edward vacuum coating system.

The structural properties of the prepared Cu_2ZnSnS_4 films were studied using Shimadzu XRD-6000 X-ray diffractometer. The microstructure of the deposited films was also examined using AA3000 atomic force microscope and structural parameters such as crystallite size and roughness were obtained. The Debye-Scherrer's formula was used to calculate crystallite size of the deposited film as follows

$$D = \frac{0.9\lambda}{\beta cos\theta} \quad (1)$$

where λ is the wavelength of the x-ray beam, β is the FWHM in radians and θ is the diffraction angle

3. Results and Discussion

The AFM images of the Cu_2ZnSnS_4 thin films deposited on a substrate with temperatures of 30, 100 and 150 °C, respectively, are shown in Fig. (2). It was found that the amorphous structure lead to decrease the reflectance, and hence to decrease the density. Therefore, a local increase in film thickness is obtained. The crystallization occurs at elevated temperatures (100 and 150°C), which is related to the reflectance increment and hence increase in film density. The well-pronounced single phase of Cu_2ZnSnS_4 at high substrate temperature (150°C) has produced much more dense crystallites arranged vertically with a size of 5.25 nm of the film. At elevated temperatures, the grain sizes decrease and exhibit much more homogeneous distribution. Table (1) summarizes the average grain size and average roughness of the prepared Cu_2ZnSnS_4 thin films.

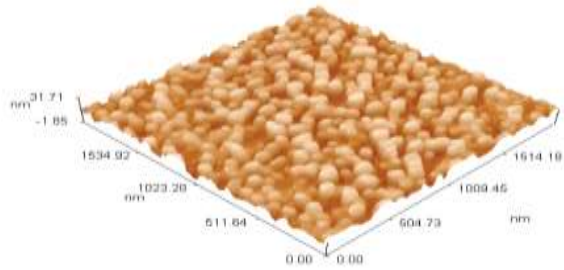

(a) 50 °C

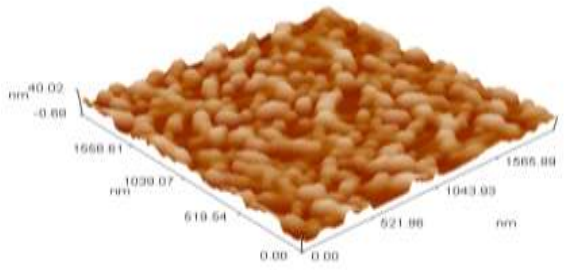

(b) 100 °C

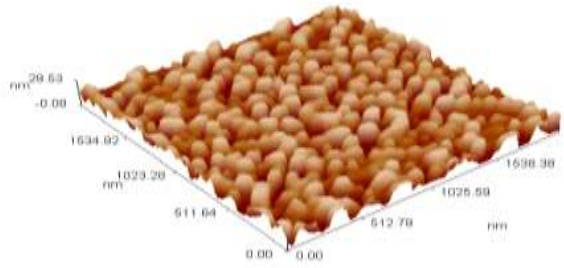

(c) 150 °C

Fig. (2) AFM images of Cu_2ZnSnS_4 thin films deposited at different substrate temperatures (50, 100 and 150 °C)

Table (1) The average grain size and average roughness of the prepared Cu_2ZnSnS_4 thin films

T_S (°C)	Grain size (nm)	Average roughness (nm)
50	66.29	3.42
100	80.53	4.73
150	77.92	5.25

Figure (3) shows the x-ray diffraction (XRD) pattern for Cu_2ZnSnS_4 alloy, which exhibits sharp peaks at 2θ of 27.492°, 27.969°, 32.027°, 43.004° and 46.291° corresponding to the reflection from (212), (111), (200), (110) and (220) planes, respectively. These reflections represent a hexagonal structure.

The XRD patterns of Cu_2ZnSnS_4 films prepared at different substrate temperatures (50, 100 and 150°C) are plotted in Fig. (4). They reveal no peaks and confirmed the amorphous structure of the as-deposited films. At elevated substrate temperatures, figure (3) shows many peaks located at 2θ of 32.346°, 43.431° and 66.649°, which correspond to the reflection from (202), (213) and (215) planes, respectively, and at 27.758° corresponding to the

reflection from (311) plane for samples deposited at the same substrate temperature. These reflections represent a tetragonal structure for samples deposited at substrate temperature of 100 and 150°C.

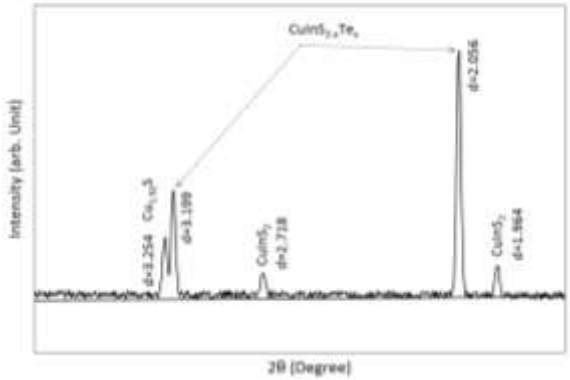

Fig. (3) The XRD pattern for Cu_2ZnSnS_4 powder extracted from films deposited on substrates

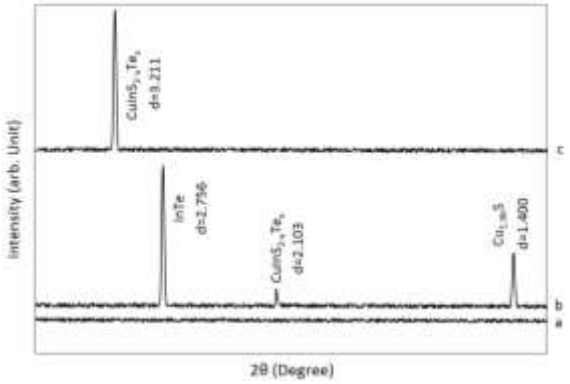

Fig. (4) The XRD patterns for Cu_2ZnSnS_4 thin films of 700nm thickness deposited at different substrate temperatures (a) 50°C, (b) 100°C and (c) 150°C

It can be concluded that the substrate temperature plays an important role in the structure behavior. Also, it is clear that the orientation of crystal peaks are low and weak at low temperature range (20-100°C), often found binary material such as CuS and ZnSn. By Comparing to high substrate temperatures, it is clearly defined and observed the sharp peaks, especially for the principal peaks on the quaternary Cu_2ZnSnS_4 compound of chalcopyrite structure oriented along the crystal plane (311) that located at 2θ of 27.783°. Since, there are no standard values available for Cu_2ZnSnS_4 compound, the XRD peaks are indexed and compared with the data of Landry et al. [24]. From table (2), the inverse relation between the grain size (D) and dislocation density (δ) can be observed. On the other hand, the grain size of Cu_2ZnSnS_4 samples deposited at 100°C (63.1 nm) is larger than that of Cu_2ZnSnS_4 powder 35.3 nm, while D of Cu_2ZnSnS_4 sample suffer abrupt reduction from 49.4 to 3.31 nm for sample deposited at 150°C. It is worthy to note that the comparison is done between the diffraction peaks that located at 32.346° and 27.647°.

Table (2) The X-ray diffraction data 2θ, d, $(I/I_o)_{exp.}$, δ, FWHM and D for Cu_2ZnSnS_4 powder and 700nm thin films deposited at different substrate temperatures (50, 100 and 150°C)

Samples	$2_{exp.}$ (deg)	$d_{exp.}$ (Å)	$(I/I_o)_{exp}$	FWHM (deg)	D (Å)	δ x10^{-5} (Å)$^{-2}$
powder	27.492	3.254	23%	0.1956	417.58	0.573
	27.969	3.199	43%	0.1655	494.79	0.408
	32.027	2.718	9%	0.2346	353.26	0.801
	43.004	2.056	100%	0.1620	529.11	0.357
	46.291	1.964	13%	0.1774	487.02	0.422
Films T_S=50°C	**Amorphous**					
Films T_S=100°C	32.346	2.756	100%	0.1310	631.89	0.25
	43.431	2.103	9%	0.1700	503.41	0.394
	66.649	1.400	39%	0.2873	331.22	0.911
Films T_S=150°C	27.647	3.211	100%	2.4675	33.180	9.1

Figure (5) shows the scanning electron microscopy (SEM) images for Cu_2ZnSnS_4 alloy samples deposited as thin film on substrates of different temperatures (50, 100 and 150°C). It is clear that the surface of the Cu_2ZnSnS_4 film deposited at substrate temperature of 50 °C is containing of particles with inhomogeneous distribution of both size and density. As well, the polycrystalline structure is confirmed in accordance to the XRD pattern of this sample. Some voids are also observed due to the inefficient alloying step of the quaternary compound during the deposition process. For the Cu_2ZnSnS_4 film deposited at substrate temperature of 100 °C, the differences in particle sizes are much more apparent while the particles get larger and increasingly diffused together. The inhomogeneity in particle size and density over the film surface is apparently higher, which is attributed to the effect of higher temperature of the substrate on which the film is deposited. Due to small thickness of the deposited Cu_2ZnSnS_4 film and the thermal effect associated to increasing substrate temperature, the growth of certain crystal planes increases whereas the growth of other crystal planes is limited or restricted. Therefore, the surface exhibits higher degree of roughness in agreement to the AFM result. As the substrate temperature is increased to 150 °C, the interstitial voids are reasonably disappeared due to the higher diffusion between particles showing higher inhomogeneity in size and distribution. Consequently, the surface roughness is decreased in agreement to the AFM result as the vacancies over the polycrystalline structure are filled with smaller particles and hence lowering the difference between the highest and lowest points over the surface.

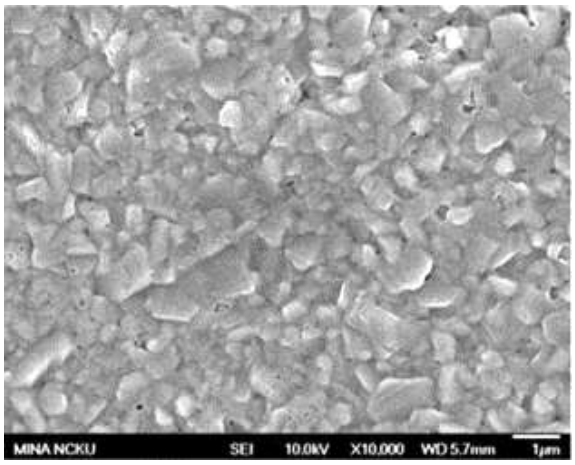

50°C

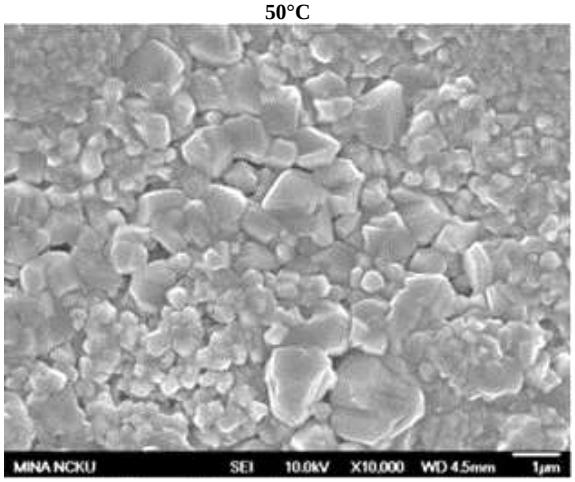

100°C

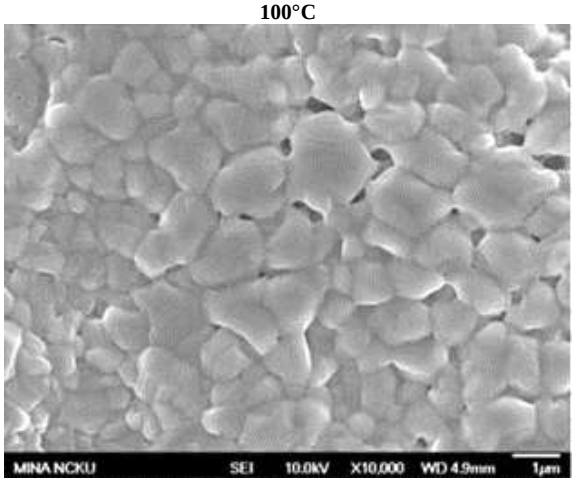

150°C

Fig. (5) The SEM images for Cu_2ZnSnS_4 powder extracted from films deposited on substrates of different temperatures

4. Conclusions

From the results obtained from this work, it can be concluded that the single phase with chalcopyrite structure of Cu_2ZnSnS_4 becomes more pronounces at elevated temperatures.

References

[1] B.A. Hasan and D.A. Umran, Semicond. Sci. Technol. 27 (2012) 125014(6pp).
[2] B.A. Hasan, Int. J. Thin Film Sci. Tech., 2(1) (2013) 29-36.
[3] R. Diaz , M. Leon , and F. Reuda, J. Vac. Sci. Technol. A 10 (1992) 295–300.
[4] K. Inakoshi, T. Ohashi, Y. Hashimoto, and Kentaro Ito, Solar Energy Mater. Solar Cells, 50(1) (1998) 37-42.
[5] K. Subbaramiah and V. Sundara Raja, Thin Solid Films, 208 (1992) 247-251.
[6] T. Ohashi, A. J. Ger, T. Miyazawa, Y. Hashimoto and K. Ito, Jap. J. Appl. Phys., 34 (1995) 4159-4166.
[7] S. Kuranouchi and T. Nakazawa, Solar Energy Mater. Solar Cells, 50 (1998) 31-36.
[8] L.I. Soliman and T.A. Hendia, Rad. Phys. Chem., 50(2), 1997, 175-177.
[9] L. Soliman, T. HendIia and H. Zayed, Fizika A (Zagreb), 16(1) (2007) 39-46.
[10] J.Y.W. Seto, J. Electrochem. Soc., 122(5) (1975) 701-706. doi: 10.1149/1.2134296
[11] S. Kumar, B. Prajapati, S.Tiwari and V. Tiwari, Indian J. Pure Appl. Phys., 46 (2008) 198-203.
[12] A.K. Jonscher, J. Phys. D: Appl. Phys., 32(14) (1999) R57-R70. DOI: 10.1088/0022-3727/32/14/201
[13] Z. Ahmad, **"Polymeric Dielectric Materials"**, Ch. 1 (2014) p. 4, doi: 10.5772/50638.
[14] L.M. Peter, Phil. Trans. Royal Soc. of London A: Math. Phys. Eng. Sci., 369(1942) (2011) 1840-56.
[15] M.A. Green et al., Prog. in Photovolt., 22(1) (2014) 1-9.
[16] B.A. Schubert et al., "An economic approach to evaluate the range of coverage of indium and its impact on indium based thin-film solar cells—recent results of Cu_2ZnSnS_4", 23rd EU-PVSEC; 2008; Valencia.
[17] B.-A. Schubert et al., Prog. in Photovolt.: Res. Appl., 9(1) (2011) 93-6.
[18] D.B. Mitzi et al., Sol. Ener. Mater. Sol. Cells., 95(6) (2011) 1421-36.
[19] K.L. Chopra, P.D. Paulson and V. Dutta, Prog. in Photovolt.: Res. Appl., 12(2-3) (2004) 69-92.
[20] S. Chen et al., Appl. Phys. Lett., 96(2) (2010) 021902.
[21] C. Yan et al., J. Alloys Comp., 610 (2014) 486-91.
[22] R. Bari and L. Patil, Sens. Transd., 125 (2011) 213-219.
[23] S. Sze and K. Kwok, **"Physics of Semiconductor Devices"**, 3rd ed., John Wiley & Sons, Inc. (New Jersey, 2007).
[24] C. Landry, J. Lockwood and R. Barron, Chem. Mater. 7(4) (1995) 699-706.

Iraqi Journal of Applied Physics

P. O. Box 55259, Baghdad 12001, IRAQ
www.iraqiphysicsjournal.com
Email: info@iraqiphysicsjournal.com
Email: editor_ijap@yahoo.co.uk
Email: irq_appl_phys@yahoo.com

Subject Index 2005-2021

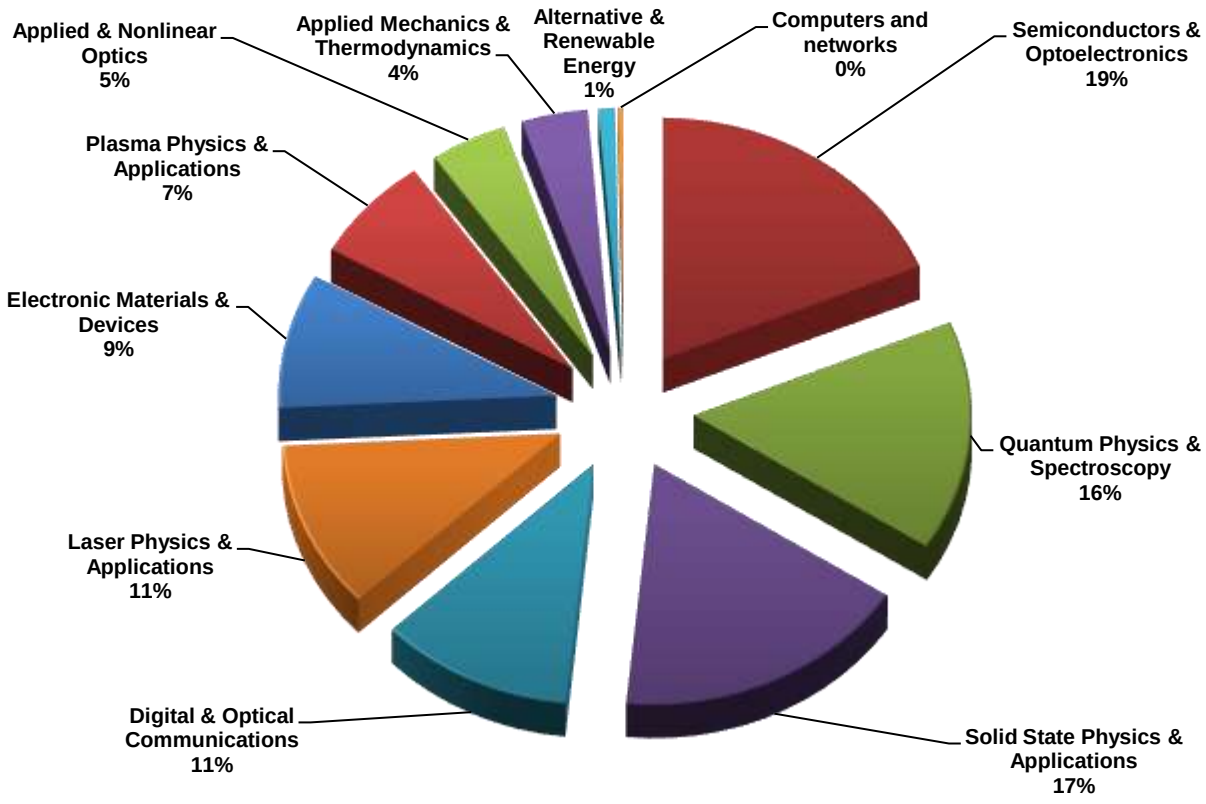

Alternative & Renewable Energy

IJAP-AARE

- General Characteristics of High Energetic Proton Events Observed with SOHO/ERNE During Solar Cycle 23, 10(4), 3
- Nuclear Green Energy, 10(1), 3
- Characterization of Laser-Ablated Nanostructured Al_2O_3/p-Solar Cells, 11(1), 29

Applied & Nonlinear Optics

IJAP-AANO

- Computer Aided Design of a Magnetic Lens Using a Combined Dynamic Programming and Artificial Intelligence Technique, 10(1), 33
- Control of Nonlinear Dynamics in Semiconductor Laser with Optoelectronic Feedback, 15(1), 3
- Curvelet-Based Optical Flow Estimation Algorithm Based on Central Derivatives, 6(2), 13
- Design of a Multi-Electrode Immersion Lens for Ion-Optical Systems, 2(1,2), 27

 ISSN (printed) 1813-2065, (online) 2309-1673 Printed in IRAQ

- Design of All-Reflecting Aplanatic Objective, 9(3), 19
- Development of an Inverted Optical Tweezers with Full Motional Control, 7(2), 19
- Investigations of Linear and Nonlinear Optical Properties of Transparent ZnO Thin Films Grown by Sol-Gel Method, 6(3), 29
- Key Mechanisms of the Nonlinear Amplification: Physics and Applications, 1(2), 3
- Microstructual Features and Properties of High-Hardness and Heat-Resistant Dispersion Strengthened Copper by Reaction Milling, 8(4), 3
- New Method for Calculating Cumulative Line Energy Using Pupil Function Technique, 2(1,2), 7
- Numerical Analysis of Temperature Dependencies of Optical Elasticity Coefficient on Lens Induced in Solid-State Laser Crystal, 14(2), 35
- Some Optical Properties of an Electrostatic Immersion Lens Using the Charge Density Method, 1(4), 21
- Temperature-Dependent Birefringence Properties of $Be_3Al_2Si_6O_{18}$ Crystal, L2(1), 12
- Thermogravimetric Properties of Porcelain Supported by Addition of Beryllium Oxide, 17(3), 27

Applied Mechanics & Thermodynamics
IJAP-AMAT

- Analytical and Experimental Study on Bound and Free Surface Waves in Wind-Wave Tank System, 8(1), 11
- Analytical Calculation of Heat Conduction in Two-Phase Heterogeneous Materials, 7(4), 11
- Characterization of D.C. Sputtering System, L1(1), 3
- Employing Inner Triplet Upgrade in Cold Mass Cooling Design for Large Hadron Collider, L2(1), 19
- HAZ Extent Analysis in Fiber-Reinforced Plastic Grooving by Laser, 1(1), 3
- Investigation of Bound and Free Surface Waves in Microwave and Acoustic Wind-Wave Tank Systems, 14(2), 11
- Optimization of Composition, Structure and Characteristics of Metal in Arc Deposition, 5(2), 37
- Marangoni Convection Effect on the Melting of GaSb/InSb/GaSb Sandwich Structured Sample, 4(2), 35
- Modeling of the Preheating Effect on Keyhole Laser Welding Efficiency, L1(1), 10
- Structural, Electronic and Thermal Properties of TiC Compound in Sodium Chloride Structure, 11(1), 9
- Torque and Magnetic Flux Analysis Using an Advanced Dynamic Dynamometer Test Bed for Electromechanical Motors, 5(1), 13
- Using Longitudinal Surface Acoustic Waves for Non-Destructive Testing of Inner Surfaces, L1(2), 9

Digital & Optical Communications
IJAP-DAOC

- A Balanced Backoff Algorithm for IEEE802.11 Wireless Network, 8(1), 27
- A CPW-Fed Printed Monopole Ultra-Wideband Antenna with E-Shaped Notched Band Slot, 6(4), 17
- A New Fractal Microstrip Bandpass Filter Design Based on Dual-Mode Square Ring Resonator for Wireless Communication Systems, 5(1), 7
- A Novel Secure Digital Watermark Generation from Public Share by Using Visual Cryptography and MAC Techniques, 10(3), 3
- Analysis and Design of Combined Fractal Dipole Wire Antenna, 5(2), 29
- Application of Multiple Coded Frame Temporal Processing to Enhance Digital Image Transfer for High-Definition Communications Systems, 14(1), 27
- Classification of Digital Modulation Using Wavelet Transform, 1(3), 15
- Coherent Detection in Optical Fiber Systems, 3(1), 3
- Comparative Evaluation of Bit Error Rate in Frequency Selective Fading Channels Employed in Wavelet Modulation, L1(2), 14
- Crosstalk and Noise in Optical Amplifier with Gain Clamping by Vertical Laser Field, 16(2), 17
- Design and Analysis of Special Small Size Cross Dipole Antenna, 6(2), 19
- Design and Implementation of Adaptive Antenna System in a New LTE 3GPP Transceivers Based Multiwavelet Signals, 10(2), 11
- Design and Implementation of Adaptive Antenna System in Physical Layer CDMA Transceivers Based Multiwavelet Signals, 11(1), 3
- Design of Low-Cost Multi-Waveforms Signal Generator Using Operational Amplifier, 14(1), 13
- Determination of The Satellite Images Orientation Using DCT Coefficients, 6(2), 31
- Dipole Antenna with Fractal Koch Curve Geometry for Multiple Frequency Applications, 7(2), 3
- Effect of Chirping on Received Pulse Shape in Optical Fiber Communications, L2(2), 7
- Frequency-Selective Surface for Reduced Mutual Coupling among Closely Spaced Array Antenna, 14(1), 19
- FSK Transceiver for Bit Error Rate Tester Implementation, 8(4), 9
- Influence of Magnetic Saturation on Sensorless Rotor Position Estimation in IPMSM Drives Based on HIL Simulator, 8(3), 3
- Linear Adaptive Antenna Array Geometry Effects on Radiation Pattern, L3(1), 3
- New Algorithm for High Throughput of IEEE 802.11 Distributed Coordination Function, 14(2), 27
- Novel Optical Fiber Sensor Based on SGMS Fiber Structure for Measuring Refractive Index of Liquids and Gases, 7(4), 17
- Probabilistic Roadmap, A*, and GA for Proposed Decoupled Multi-Robot Path Planning, 10(2), 3
- Performance Optimizing of Fourth Order Delta-Sigma Fractional-N Frequency Synthesizer using a Dither Technique for Third Generation (3G) Applications, 7(1), 3
- Phase Noise Compensation for Coherent Orthogonal Frequency Division Multiplexing in Optical Fiber Communications Systems, 5(2), 3
- Quantum Limit Characterization of Signal-to-Noise Ratio using Phase-Shift Keying in Homodyne Detection, L3(1), 11
- Range-Coverage Extension Using Smart Antennas in Mobile Communications Systems, 5(2), 25
- Reliable Implementation of Paillier Cryptosystem, 10(4), 27
- Signal Mechanism Analysis of Fiber Arrival Time in Fiber Optic Pin, 5(2), 13
- Software Defined Radio (SDR) Methodology Based Multi–Core Software Platform, 9(4), 3
- Synchronization Scheme for Secured Communications System Based on Chaotic Signals, L3(1), 7
- Transmission of Compressed Video Signals through Spread Spectrum Channel, 6(4), 9
- A Method to Improve the Security Level of Advanced Encryption Standard Algorithm by Using Proposed Algorithm, 8(4), 29

Electronic Materials & Devices
IJAP-EMAD

- Analysis of Atomic and Electronic Structures of NiO/Au Interfaces by High-Resolution MEIS and Photoelectron Spectroscopy, 14(3), 13
- Characterization of E-Mode InZnO Thin Film Transistors Produced by DC Sputtering Technique, L3(1), 19
- Comparison of Electro-optical Effects in Pure and Cobalt Nanoparticles-Doped 6CHBT Liquid Crystals, 15(1), 5
- Dark and Illumination Electrical Characteristics of ZnS/Si Heterojunction Prepared by Pulsed Laser Deposition, 11(2), 25
- Determination of Electronic Properties of Gallium Nitride Structure Using Density Functional Theory, 17(4), 19
- Development of NVD's Using XR5™ IIT Technique and III-V Photocathode Under Night Sky Conditions, 7(4), 33

Laser Physics & Applications

IJAP-LPAA

Plasma Physics & Applications

IJAP-PPAA

 ISSN (printed) 1813-2065, (online) 2309-1673 Printed in IRAQ

- Current-Voltage Characteristics of DC Plasma Discharges Employed in Sputtering Techniques, 12(3), 10
- Determination of Electron Temperatures in Rare-Gases Plasma, 4(1), 5
- Effect of Adding Nitrogen to the Gas Mixture on Plasma Characteristics of a Closed-Field Unbalanced DC Magnetron Sputtering System, 10(1), 27
- Effect of Annealing on the Electrical Characteristics of CdO-Si Heterostructure Produced by Plasma-Induced Bonding Technique, 4(3), 33
- Employment of Magnetron to Enhance Langmuir Probe Characteristics of Argon Glow Discharge Plasma in Sputtering System, 12(4), 19
- Generation of Highly-Directed Laser-Driven Plasma Blocks for Light Ion Beam Fusion Applications, 6(1), 3
- Influence of Inter-Electrode Distance, Gas Mixing, Magnetic Field and Cathode Material on Breakdown Voltage of Lab-Made DC Magnetron Sputtering Device, 10(4), 21
- Influence of Magnetic Nitrogen Plasma Functionalization of High Density Polycarbonate, 8(4), 17
- Isentropic and Isenthalpic Cooling Techniques for Low-Temperature Discharges, 15(4), 29
- Langmuir Probe Diagnostics of Low-Pressure Glow Discharge Plasma Using Argon-Nitrogen Mixtures, 12(2), 17
- Laser-Based Measurements in Non-Equilibrium Plasmas, 8(1), 3
- Magnetic Field Distribution of Closed-Field Unbalanced Dual Magnetrons Employed in Plasma Sputtering Systems, 12(3), 35
- Microhardness and Tension Measurements of Pulsed-Laser Surface-Treated Aluminum Alloys, 11(3), 21
- Monte Carlo Simulation of Electronic Kinetics in Gas Discharge, 1(3), 3
- Numerical Model to Estimate the Potential Changes within Laser-Solid Surface Interaction Zone, 6(2), 3
- One-Dimension Simulation of Plasma Flow in the Cylindrical Hall Thruster, 8(4), 23
- The Fundamentals of Plasma-Assisted CVD Technique Employed in Thin Films Production, L1(2), 3

Quantum Physics & Spectroscopy

IJAP-QPAS

- Alternative mechanisms for electroweak symmetry breaking, 8(2), 8
- Application of Hydrotropic Solubilization Phenomenon for Estimating Diacerein in Capsule Dosage Form by Spectrophotometry Methods, 8(3), 17
- Beating Classical and Quantum Limits in Optics, 3(2), 3
- Calculation of Charge Density Distribution of (2s-1d) Shell-Model Nuclei Using the Occupation Numbers of States, 2(1,2), 31
- CERN experiments observe particle consistent with long-sought Higgs boson, 8(3), 11
- Characterization of Highly-Pure Silicon Dioxide Nanoparticles as Scattering Centers for Random Gain Media, 16(2), 37
- Correction Four-Component Dirac-Coulomb Using Gaussian Basis-Set and Gaussian Model Distribution for Super Heavy Element (Z=115), 12(1), 17
- Design of a Fundamental Concept of Virtual Reality System for Intensity Distribution in Free Electron Laser Amplifier, 4(1), 11
- Dispersion Compensation for a Femtosecond Self-Pumped Phase Conjugator, 2(3,4), 9
- Effect of Acidic Environment on the Spectral Properties of *Hibiscus sabdariffa* Organic Dye used in Dye-Sensitized Solar Cells, 10(2), 27
- Effect of Dissipative Forces on the Theory of a Single-Atom Microlaser, 2(3,4), 12
- Effect of Oxygen Quencher on Absorption and Fluorescence Spectra of Rhodamie-6G and Rhodamine-B Dyes in Ethanol Solvent, 1(1), 20
- Effect of the Scattered Solar Radiation on the Atmospheric Ozone Measurements, 2(1,2), 11
- Effect of Thermal Annealing on Photoluminescence Characteristics of Titanium Dioxide Thin Films Doped with Copper Oxide by Pulsed-Laser Deposition, 17(4), 15
- Effective Collection and Transformation of Emission into Directional Radiation Based on Surface Plasmon-Coupled Emission, 17(1), 21
- Effects of Rare Earth Dopants on Spectroscopic Properties of Silica Glasses Prepared by Sol-Gel Technique, 16(3), 3
- Effects of Solvent Properties on Absorption and Fluorescence Characteristics of Two Organic Dyes Used as Random Gain Media, 17(2), 15
- Effects of Temperature and Concentration on Spectroscopic Behaviors of Laser Dye, 12(1), 35
- Elusive particle may be near, 8(2), 26
- Energy Transfer Calculations Based on Fluorescence Spectra of Acriflavine and Rhodamine B Laser Dyes, 16(3), 33
- Experimental Observations and Modelling of Electron Density of the Plasmasphere, 6(1), 47
- Extra Val Function for the Theoretical Sensing of Ultraviolet Light and Temperature Produced by Fluorescein-Filled Photonic Crystal Fiber, 13(3), 29
- Fluorescence Energy Transfer Characteristics in Binary Acriflavine-Red Nut Lasing Dye Mixtures, 12(2), 3
- Fractal Nanotechnology, 4(4), 25
- FTIR Spectra of Molybdenum Tellurite Glasses, 2(1,2), 23
- FTIR Spectroscopic and Computational Studies on Hydrogen Adsorption on the Zeolite Li–FER, 4(2), 21
- General Characteristics of High Energetic Proton Events Observed with SOHO/ERNE During Solar Cycle 23, 10(4), 3
- Generation of Femtosecond Pulses from Order-of-Magnitude Pulse Compression in a Synchronously Pumped Optical Parametric Oscillator Based on Periodically Poled Lithium Niobate, 2(3,4), 24
- Generation of Intense 8-fs Pulses at 400nm, 2(3,4), 15
- Higgs Boson, 8(2), 3
- High-Intensity Third-Harmonic Generation in Beta Barium Borate Through Second-Order and Third-Order Susceptibilities, 2(3,4), 18
- Introduction to the Higgs Boson Papers, 8(2), 12
- Introduction to Particle Physics and the LHC, 8(2), 23
- Luminescence Characterization of the Bio-Conjugated Quantum Dots with CA125 Antigen Using Linkage Molecules, 7(1), 27
- Luminescent Plates Doped with Stilbene 420 Dye for Enhanced Silicon Solar Cell Performance: Down-Conversion, 6(4), 3
- Measurements of *d*-band Center Shifts of Titanium Dioxide Catalyst Using Gold Nanoparticles in Carbon Monoxide Oxidation Reaction, 14(3), 3
- Measurement of Water Vapour and Temperature Profiles Within the Troposphere Using Ultraviolet Raman LIDAR System, 8(1), 19
- Medium Energy Ion Scattering Spectrometry of Helium Ions Scattered from Rutile Titanium Dioxide Surfaces, 14(3), 29
- Nanolasers: Lasing from Nanoscale Quantum Wires, 3(4), 3
- Near-Edge X-ray Absorption Fine Structure Analysis of Magnesium-Palladium Nanoparticles Fabricated by Gas Evaporation Method, 14(3), 35
- Optimization and Fine-Tuning of Controlled White-Light Continuum Generation in Transparent Solid Medium by 1-kHz Repetition Rate Femtosecond Laser Pulses, 12(1), 27
- Phase Conjugation with Random Fields and with Deterministic and Random Scatterers, 2(3,4), 21
- Preparation and Characterization of Dysprosium-Doped Titanium Dioxide Photocatalyst by Sol-Gel Method, 17(3), 3
- Silicon Dioxide Nanostructures-Coated External Cavity for Gain Enhancement of Rhodamine B Lasing Dye, 14(1), 3
- Some Physical Properties of Metal-Hydroxyquinoline Complexes in Different Solvents, 17(1), 9
- Spectroscopic Study of Chromium-Doped Silicon Nitride Nanostructures Prepared by DC Reactive Magnetron Sputtering, 17(2), 11
- Synchronization in Optically Coupled Chaotic Systems by Optical Feedback, 12(1), 11

- Synchrotron-Radiation Infrared Microscopy Analysis of an Amyloid Peptide Irradiated by Mid-Infrared Free-Electron Laser, 14(3), 41
- The biggest machine in the world, 8(2), 22
- The Mythical Higgs Boson, 8(2), 26
- Finding the Smallest Unifying Particle in the Human Universe: An Artistic Theory of Everything, 8(2), 27
- X-Ray Absorption Fine Structure Spectroscopy of Alumina-Supported Copper Oxide for Conversion Electron Yield Detection, 14(4), 29

Semiconductors & Optoelectronics

IJAP-SCAOE

- Analysis and Simulation of Carrier Transport in InP-Based Double Heterojunction Photoelectronic Device, 13(3), 23
- Annealing Effect on the Photoluminescence of CdTe/CdSe Thin Film Photovoltaic Devices, 1(3), 23
- Band Diagram of p-PbTe/n-Si Heterostructure, 1(2), 27
- Characteristics of a-Si:H Solar Cell Under Extended Illumination Condition Using NIR Laser, 5(1), 35
- Characteristics of p-n Junction Silicon Carbide LED, 2(1,2), 17
- Characterization of $(CdO)_{1-x}(ZnO)_x$ Thin Films Prepared by Pulsed-Laser Deposition for Solar Cell Applications, 11(3), 3
- Characterization of CdS:In/Si Heterojunction Solar Cells, 1(2), 13
- Characterization of SiC/Si Heterojunction Fabricated by Plasma-Induced Growth of Nanostructured Silicon Carbide Layer on Silicon Surface, 12(2), 9
- Charge Injection into Organic Semiconductors, 4(2), 5
- Computation of Optical Energy Gap of Cu_2O Thin Film: Theoretical Estimation, L1(1), 21
- Correlation Between Kinematics, Optical and Structural Properties of Size Quantized PbS Nano Films Deposited by Spray Pyrolysis, 10(3), 35
- DC Conductivity and Optical Properties of $InSbTe_3$ Amorphous Thin Films, 6(3), 9
- Density of Defect States in $Se_{90}Sb_{10-x}Ag_x$ Glassy Alloys, 9(4), 25
- Determination of Energy Band Outline of CoO:Au/Si Thin Film Solar Cells, 17(3), 17
- Effect of Annealing Temperature on Urbach Energy for $CdO:In_2O_3$ Thin Films Prepared by Pulsed-Laser Deposition, 16(1), 21
- Effect of Bath Temperature on the Optoelectronic Characteristics of Chemically Deposited CdS Thin Films, 5(1), 23
- Effect of pH Value on the Photoconductivity of Chemically Deposited CdS Thin Films, L2(1), 23
- Effect of Thickness on Optical and Electrical Properties of ZnO Prepared by CBD, 7(1), 11
- Effect of Using Organic Stabilizing Agent on Structural Characteristics of Cadmium Telluride Quantum Dots, 17(3), 13
- Effects of Deposition Parameters on Chemically Deposited PbS Thin Films, 4(4), 7
- Effects of Temperature on The Properties of Amorphous-to-Crystalline Transition in $AgSbSe_2$ Thin Films, 7(1), 17
- Efficiency Enhancement of Photovoltaic Silicon Cell by Ultrashort Laser Pulses, 5(2), 33
- First Principle Calculation of Pressure-Induced Phase Transition and Band Structure of Gallium Phosphide, 9(4), 17
- Gas Phase Growth Techniques for Quantum Dots: An Overview, 14(4), 3
- Growth of $In_xGa_{1-x}Sb$ Bulk Crystals by Czochralski Technique, 1(4), 17
- Heterojunction Solar Cell Based on Highly-Pure Nanopowders Prepared by DC Reactive Magnetron Sputtering, 16(3), 27
- High-Quality Plasma-Induced Crystallization of Amorphous Silicon Structures, 5(1), 35
- Illumination and Dark Current-Voltage Characteristics of Polymer-Silicon Heterojunction Solar Cells, L2(1), 12
- Influence of Deposition Parameters on Optical and Electrical Properties of Cu_xS Thin Films Prepared Using Chemical Bath Deposition Method, 4(3), 19
- Investigation of Amorphous to Crystalline Transition in Glassy $Se_{80}Te_{20}$ and $Se_{70}Te_{20}M_{10}$ (M=Ag, Cd, Sb) Alloys, 1(3), 7
- Light-Beam-Induced-Current Analysis of Thin-Film Polycrystalline Solar Cells, 7(4), 29
- Modeling of Transport Properties of Amorphous Silicon Solar Cells, 6(1), 25
- Nano/Micro Surface Texturing and Enhancing of Photovoltaic Cells Efficiency by Using UV Femtosecond Laser Pulses, 7(2), 33
- Nickel Doping and Annealing Effects on the Structural and Optical Properties of Iron Oxide Thin Films, 10(3), 17
- Optical and Electrical Properties of Zinc Oxide Films Prepared by Spray Pyrolysis, 6(4), 23
- Optical and Electrical Properties of ZnO Thin Films Prepared by Spray Pyrolysis Technique, 4(1), 31
- Optical Properties of Annealed Cadmium Sulfide Thin Films Prepared by Chemical Bath Deposition, L2(2), 19
- Optical Properties of Many-Layers Zinc Sulphide Thin Films prepared by Chemical Bath Deposition Method, 6(3), 33
- Optical Properties of Thermally-Annealed Tin-Doped Indium Oxide Thin Films, L2(2), 15
- Optimization of Silicon Solar Cells Efficiency by Chemical Texturing, 10(2), 17
- Optoelectronic Characteristics of As-doped Silicon Photodetectors Produced by LID Technique, L1(2), 23
- Photocatalytic Performance of Mixed and Single Phases of Titanium Dioxide Nanoparticles on Growth of Fusarium Oxysporum Fungal, 17(4), 9
- Preparation and Characteristic Study of In_2O_3/c-Si Made by Spray Pyrolysis, 1(1), 11
- Preparation and Characterization of Self-Assembled n-ZnS Thin Films, 4(4), 33
- Preparation and Characterization of PAni Films by Electrochemical Polymerization, 10(2), 23
- Preparation and Study of Indium Oxide Nanoparticles, 10(4), 15
- Spectral and Electrical Characteristics of Nanostructured NiO/TiO_2 Heterojunction Fabricated by DC Reactive Magnetron Sputtering, 16(3), 39
- Stress Management and Interfacial Strength of Gallium Nitride Layer Grown on Diamond Substrate, 13(2), 19
- Structural Characteristics of Silicon Nitride Nanostructures Synthesized by DC Reactive Magnetron Sputtering, 15(4), 33
- Structural, Electronic and Gas Sensing Properties of Cu-Doped ZrO_2-TiO_2, 10(3), 23
- Structural Properties of Semiconducting Nanostructures Prepared by DC Plasma Reactive Sputtering Method, 10(3), 41
- Studying Defects on Semiconductor Surfaces by Photoacoustic Spectroscopy, 6(3), 25
- Synthesis of Silicon Nanowires by Selective Etching Process, 4(3), 15
- Technology and Future of III-V Multi-Junction Solar Cells, 6(3), 3
- The Effect of Some Experimental Parameters on the Properties of Porous Silicon, 4(1), 37
- Theoretical Treatment to Determine the Quality of Photonic Crystal Fiber (PCF) as a Function of the Number of Air Holes, 9(3), 31
- Thermal Management of Vertical External Cavity Surface Emitting Laser Grown on GaAs Substrate, 13(2), 15
- Thermally Stimulated Currents Technique to Study Traps in Insulators and Semiconductors, 11(2), 3
- Using Substrate Removal Technique for GaAs-Based VECSEL Optimization, 13(2), 23

Solid State Physics & Applications

IJAP-SSPAA

- A Mathematical Model to Describe the Densification Process During the Sintering of Ceramic Compacts, 4(2), 11
- Antibacterial Activity of Gold and Silver Nanoparticles against Pathogen Species, *E. coli* and *S. aureus*, 13(3), 19

 ISSN (printed) 1813-2065, (online) 2309-1673 Printed in IRAQ

* * *

Notes:

- 1(1), 3 refer to IJAP, Vol. 1, No. 1, page 3
- L1(1), 3 refer to IJAPLett, Vol. 1, No. 1, page 3

Iraqi Journal of Applied Physics

P. O. Box 55259, Baghdad 12001, IRAQ
www.iraqiphysicsjournal.com
Email: info@iraqiphysicsjournal.com
Email: editor_ijap@yahoo.co.uk
Email: irq_appl_phys@yahoo.com

Author Index 2005-2021

 ISSN (printed) 1813-2065, (online) 2309-1673 Printed in IRAQ

 ISSN (printed) 1813-2065, (online) 2309-1673 Printed in IRAQ

 ISSN (printed) 1813-2065, (online) 2309-1673 Printed in IRAQ

THE IRAQI JOURNAL OF APPLIED PHYSICS
EDITORIAL BOARD

COPYRIGHT RELEASE FORM
IRAQI JOURNAL OF APPLIED PHYSICS (IJAP)

We, the undersigned, the author/authors of the article titled

……
……
……
……
……
……
……

that is submitted to the Iraqi Journal of Applied Physics (IJAP) for publication, declare that we have neither taken part or full text from any published work by others, nor presented or published it elsewhere in any other journal. We also declare transferring copyrights and conduct of this article to the Iraqi Journal of Applied Physics (IJAP) after accepting it for publication.

The authors will keep the following rights:

1. Possession of the article such as patent rights.
2. Free of charge use of the article or part of it in any future work by the authors such as books and lecture notes after informing IJAP editorial board.
3. Republishing the article for any personal purposes of the authors after taking journal permission.

To be signed by all authors:

Signature:……..date: ……
Printed name: ……

Signature:……..date: ……
Printed name: ……

Signature:……..date: ……
Printed name: ……

Correspondence
address:……...
……
Address:……
……
Telephone:……..……email: ……

Note: Complete and sign this form and mail it to the below address with your finally revised manuscript

The Iraqi Journal of Applied Physics
www.iraqiphysicsjournal.com
Email: info@iraqiphysicsjournal.com
Email: editor_ijap@yahoo.co.uk
Email: irq_appl_phys@yahoo.com

IRAQI JOURNAL OF APPLIED PHYSICS

Volume (17), Issue (4), October-December 2021

CONTENTS